View Article Online
View Journal

INORGANIC
CHEMISTRY

FRONTIERS

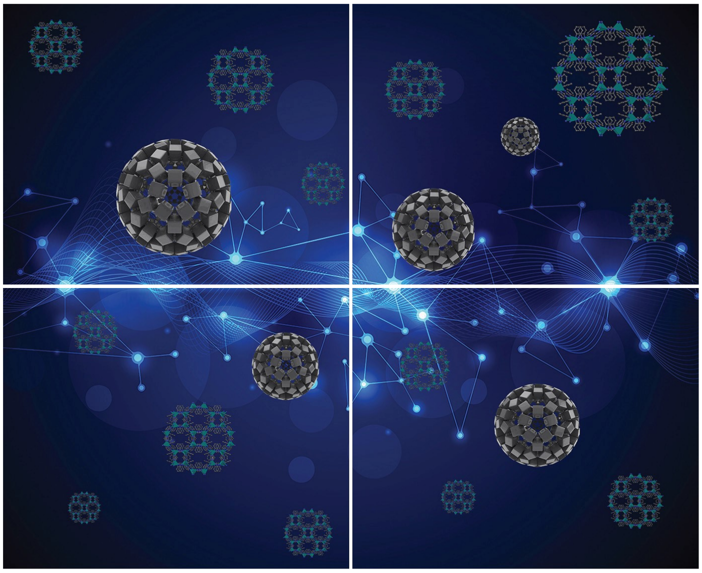

This article can be cited before page numbers have been issued, to do this please use: S. J. Shah, R. K. Tiwari, N. Ghosh, E. Garribba, M. Ishida, G. Rajaraman, H. Furuta and S. P. Rath, *Inorg. Chem. Front.*, 2025, DOI: 10.1039/D5QI01135C.

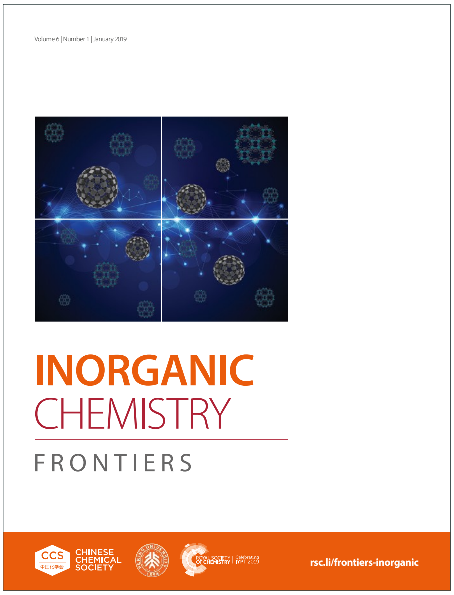

Volume 6 | Number 1 | January 2019

INORGANIC
CHEMISTRY
FRONTIERS

rsc.li/frontiers-inorganic

View Article Online
DOI: 10.1039/D5QI01135C

Received 00th xxxxxxx XXxx,
Accepted 00th xxxxxxx XXxx

DOI: 10.1039/x0xx00000x

Controlling Intramolecular Electronic Communication through the Conformation Changes via Stepwise Oxidations in Dicopper(II) and Dinickel(II) Porphyrin Dimers

Syed Jehanger Shah,[a] Rupesh Kumar Tiwari,[b] Niva Ghosh,[a] Eugenio Garribba,[c] Masatoshi Ishida,[d] Gopalan Rajaraman,[b] Hiroyuki Furuta[a,e,f] and Sankar Prasad Rath[a]*

Herein, we report a shape-dependent intramolecular electronic communication in neutral and oxidized complexes of dinickel(II) and dicopper(II) porphyrin dimers. Upon careful manipulation of the reaction conditions, nano-size molecules having different shapes, namely 'linear', 'cofacially sloping', and 'clamshell bucket', were synthesized by varying the concentration of 2,3-dichloro-5,6-dicyano-1,4-benzoquinone (DDQ). Detailed structural, spectroscopic viz. UV-vis-NIR, NMR, EPR, ESI-MS, VT magnetic study, and extensive computational investigation have been exploited to investigate long-range electronic communication. The varying shapes and extent of conjugation of the porphyrin dimers are responsible for several prominent attributes, including colours, polarity, π-conjugation, intensity of NIR absorption bands and narrow HOMO−LUMO gaps, etc. Notably, the addition of carbonyl moieties at the methine bridge in 'clamshell bucket' facilitates stronger electronic communication through it followed by the 'linear' and 'cofacially sloping' complexes. Upon stepwise oxidations, highly stable mono-cation radical and di-cation di-radicals were isolated that exhibited long-range charge/radical delocalization via the bridge to produce strong NIR bands. The spin-density plots for the neutral, 1e⁻, and 2e⁻ oxidised complexes demonstrate the crucial role of metal ions, the bridge, and their shapes in long-range electronic communication. π-Conjugation between two macrocycles in the 2e⁻-oxidized complexes is better in the linear 'butterfly-like' molecule, followed by curved 'cofacially sloping' and carbonyl-inserted 'clamshell bucket', while nickel(II) dominates over copper(II) motifs. Notably, the distinct signatures of the triplet state in the EPR spectra were observed due to the magnetic interaction between the two Cu(II) centres in the 2e⁻-oxidized complexes. The carbonyl group acts as a good π-mediator in the oxidized complex for through-space intramolecular communication between the two rings.

Introduction

Porphyrin arrays with extended electronic networks are attractive scaffolds for the development of a diverse spectrum of functional materials, near-infrared (NIR) dyes, and non-linear optical materials.[1] Because of their conjugated electronic properties, these arrays have the potential to be used as conducting molecular wires.[2c,e] Metalloporphyrin arrays continue to draw a lot of interest due to their distinctive features in design and creation.[1,2] In order to facilitate long-range electronic communication over the bridge linking the metalloporphyrin centres, these highly conjugated complexes offer a potential platform for systematic research on spin-spin coupling.[1-4] The extent of electronic coupling and the interchromophore separation are critical elements in the formation of electron and charge resonance phenomena. The ability of the redox active and conjugated bridging moiety to establish a specific shape, relative orientation, and separation between each chromophore simultaneously facilitates communication between the spin carriers[4] along with a sharp distinction in their molecular and optical properties like polarity, conjugation, luminescence, two-photon absorption, etc. Indeed, the advantage of such redox-active bridges is very intriguing since they may adjust spin communication by mild oxidation or reduction and thereby function as a very effective magnetic relay between the spins.[5]

Exploration of the strongly π-conjugated robust cation radicals has always been challenging.[6] Recently, it has been established that macrocycles can stabilize their extensively conjugated radicals due to their significant spin delocalization.[6–14] The introduction of the π-spacers between the two porphyrin units and the π-extension with core porphyrin frameworks leads to a superior stability of the π-cation radicals. Further, the increase in conjugation leads to remarkable electrochemical redox properties and peculiar electronic characteristics due to breaking the degeneracy of the frontier molecular orbitals (FMOs) and a decrease of the highest occupied molecular orbital (HOMO)–lowest unoccupied molecular orbital (LUMO) energy gap.[9] The spin coupling models in the metalloporphyrin dication diradicals are found to be dependent on the nature of the metal ion.[14]

---

[a] *Department of Chemistry, Indian Institute of Technology Kanpur, Kanpur-208016, India; Email: sprath@iitk.ac.in*
[b] *Department of Chemistry, Indian Institute of Technology Bombay, Mumbai – 400076, India.*
[c] *Dipartimento di Medicina, Chirurgia e Farmacia, Università di Sassari, Viale San Pietro, I-07100 Sassari, Italy.*
[d] *Department of Chemistry, Graduate School of Science, Tokyo Metropolitan University, Tokyo 192-0397, Japan*
[e] *Department of Applied Chemistry, Graduate School of Engineering, Kyushu University, Fukuoka 819-0395, Japan*
[f] *Center for Supramolecular Chemistry and Catalysis, Department of Chemistry, College of Sciences, Shanghai University, Shanghai 200444, P. R. China*
[g] *Electronic Supplementary Information (ESI) available: Text, Figures, and tables depicting detailed experimental procedures and characterisation data including UV-vis, X-ray crystallography and DFT. CCDC 2308954, 2444834 & 2444835. See DOI: 10.1039/x0xx00000x*

View Article Online
DOI: 10.1039/D5QI01135G

Herein, we demonstrate shape-dependent intramolecular through-bridge spin coupling in dinickel(II) and dicopper(II) porphyrin dimers in neutral as well as oxidized conjugated species formed upon stepwise oxidations. We have reported recently the synthesis of an unconjugated 5-(2,6-dichlorophenyl)dipyrromethane (DPM) bridged dinickel(II) and dicopper(II) porphyrin dimers **1**•M (M = Ni, Cu), Scheme 1.[14a] The controlled additions of 2,3-dichloro-5,6-dicyano-1,4-benzoquinone (DDQ) or *p*-chloranil to **1**•M at different reaction conditions lead to the formation of conjugated '*linear''* **2**•M, '*cofacially sloping'* **3**•M, and carbonyl mediated '*clamshell bucket'* **4**•M species (Scheme 1). The two conformational isomers, **2**•M and **3**•M, reported recently, are reversibly interconvertible by applying light and temperature,[14b] while the greenish and highly polar complex **4**•M (M = Ni, Cu) has been reported here for the first time which has been synthesized by the oxidation of **1**•M with excess DDQ oxidant.

These four different types of metalloporphyrin dimers, **1**•M, **2**•M, **3**•M, and **4**•M, are compared here based on their shape, conjugation, and spin coupling abilities. The highly π-conjugated nature and varying shapes of the porphyrin dimers give rise to various prominent attributes, such as red-shifted and highly intense NIR absorption bands, narrow HOMO–LUMO gaps, flexible conformational change, etc. These dinickel(II) and dicopper(II) porphyrin dimers, upon further oxidation, produce the corresponding one- and two-electron oxidised species exhibiting long-range charge/radical delocalization with strong NIR bands. Besides long-range communication and shape change in the case of **2**•M, **3**•M, and **4**•M, their radical cations can withstand silica gel chromatography. They can be stored for months under ambient conditions with extraordinary stability offered by π-conjugation. In sharp contrast, the dication diradical complex of the unconjugated **1**•M was highly reactive and formed a stable triply-fused π-conjugated chlorin porphyrin heterodimer.[15]

Results and discussion

Starting from 5-(*N*,*N*-dimethylamino)octaethylporphyrin metal complex (M: Ni, Cu), the 5-(2,6-dichlorophenyl)dipyrromethane-bridged porphyrin dimer **1**•M, **2**•M, and **3**•M were obtained using a procedure reported recently by us.[14a] The additions of DDQ or *p*-chloranil to **1**•M at different reaction conditions lead to the formation of conjugated **2**•Cu and **3**•Cu (Scheme 1). Interestingly, these two conformational isomers, **2**•M and **3**•M, are reversibly interconvertible by applying light and temperature, as demonstrated recently.[14b]

To understand the impact of the bridge on π-conjugation, two carbonyl groups were introduced between the dipyrrin bridge and the porphyrin chromophores to form **4**•M. The synthesis of **4**•M was done by the oxidation of **1**•M with an excess DDQ and stirring for 2 hours. The greenish, highly polar complex **4**•M was then purified through silica gel column chromatography (CH_3OH/CH_2Cl_2 = 5:95 v/v) with excellent yield as a solid. The generation of carbonyl at the methine bridge by altering the reaction conditions introduces contortion in the structure but still communicates through -C=O due to its π-acceptor ability (Scheme 1). Complexes **4**•M have been characterized using high-resolution electrospray ionization (ESI) mass spectra of **4**•Ni as $[M + H]^+$: *m/z* = 1523.5756, and **4**•Cu as $[M]^+$: *m/z* = 1533.5638 (Figures S1–S4).

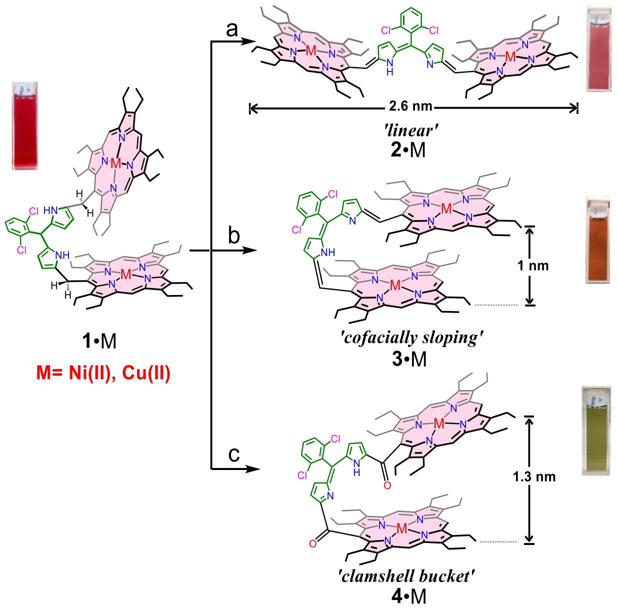

Scheme 1. Synthetic outline of the complexes and their abbreviations. Reaction conditions: (a) DDQ (2 equiv), CH_2Cl_2, 295 K, 1 h; (b) DDQ (2 equiv), CH_2Cl_2, 295 K, 30 min, and (c) DDQ (6 equiv), CH_2Cl_2, H_2O (trace amount), 295 K, 2 h. The distances highlighting the size of the molecules have been directly taken from their crystal structures.

It is interesting to note that three molecules, **2**•M, **3**•M, and **4**•M, with significant changes in their molecular architecture, were achieved just by careful manipulations of the reaction conditions, which ultimately brought disparity in their molecular properties like colour, polarity, π-conjugation, red-shifted bands in the NIR region, etc. Although the syntheses of the complexes were done in one pot just by fine-tuning the reaction conditions, they are easily separated through silica gel column chromatography due to a significant disparity in their polarity based on their conjugation abilities. **2**•M was synthesized by stirring **1**•M with two equivalents of DDQ for 1 hour, and its conformational isomer **3**•M was exclusively produced by mixing the same precursor **1**•M for only 30 minutes. However, excessive use of DDQ directly leads to the

View Article Online
DOI: 10.1039/D5QI01135C

Table 1. Selected structural and geometrical parameters of the complexes

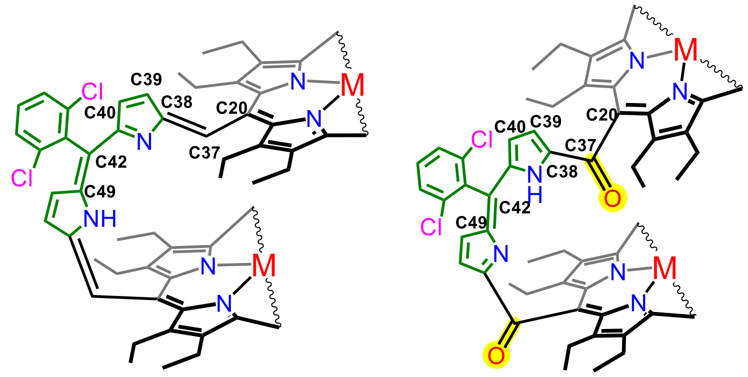

Complex	**1**•Cu	**2**•Ni	**3**•Cu	**3**•Ni	**4**•Cu·C_6H_{14}	**4**•Cu·CH_2Cl_2
M1–N_p (Å)^a	2.012(6)	1.898(5)	2.004(4)	1.928(7)	1.995(6)	1.995(3)
M2–N_p (Å)^a	2.002(7)	1.903(6)	1.997(4)	1.913(10)	1.999(7)	2.002(3)
Δ_{24} (Å)^b	0.01	0.34	0.13	0.11	0.18, 0.08	0.18, 0.04
M···M (Å)^c	9.83	16.39	7.41	7.41	8.79	8.70
C_m···C_m (Å)^d	8.61	9.94	6.69	6.61	6.78	6.69
Θ (°)^e	85.55	52.53	14.22	20.42	57.0	52.20
C20–C37 (Å)	1.503(10)	1.474(8)	1.490(7)	1.487(11)	1.517(9)	1.513(6)
C37–C38 (Å)	1.510(10)	1.331(9)	1.343(8)	1.349(12)	1.456(9)	1.452(6)
C42–C49 (Å)	1.493(10)	1.388(8)	1.363(7)	1.380(13)	1.346(11)	1.344(6)
Ref.	14a	14a	14b	This work	This work	This work

^{a}Average value. ^{b}Average displacement of atoms from the least-squares plane of the $C_{20}N_4$ porphyrinato core. ^{c}Non-bonding distance between two metal centers. ^{d}Non-bonding distance between two *meso*-carbons that are covalently connected. ^{e}Angle between two least-squares planes of the $C_{20}N_4$ porphyrinato cores.

formation of **4**•M as a major product. The wide distribution and distinction in their colour, such as **2**•M (light reddish), **3**•M (light brown), and **4**•M (light green), also makes their separation even easier.

Crystallographic characterization

Single crystals of **3**•Ni were grown by the slow diffusion of *n*-hexane into the dichloromethane solution of the complex at room temperature in the air. Similarly, single crystals of **4**•Cu were also grown from two different solvent mixtures: in one set, the dichloromethane solution of the complex was layered with cyclohexane to produce **4**•Cu·CH_2Cl_2, and, in another set, the benzene solution of the complex was layered with *n*-hexane to produce **4**•Cu·C_6H_{14}. All the structures were unambiguously elucidated by X-ray crystallographic analysis. Figure 1 displays the X-ray structures of the complexes, while their molecular packings in the unit cells are shown in Figures S5–S7. The crystallographic data and data collection parameters of the complexes are shown in Table S1.

In **3**•Ni, the porphyrin planes are slipped and nearly cofacial to each other with a dihedral angle of 20.42° and a Ni•••Ni nonbonding distance of 7.41 Å. The average Ni−Np distances (Np = pyrrole nitrogen atom of the porphyrin) in the two porphyrin cores are 1.928(7) Å and 1.913(10) Å, respectively, which fall within the range observed for four-coordinate Ni(II) porphyrinates **3**•Ni displays a planar

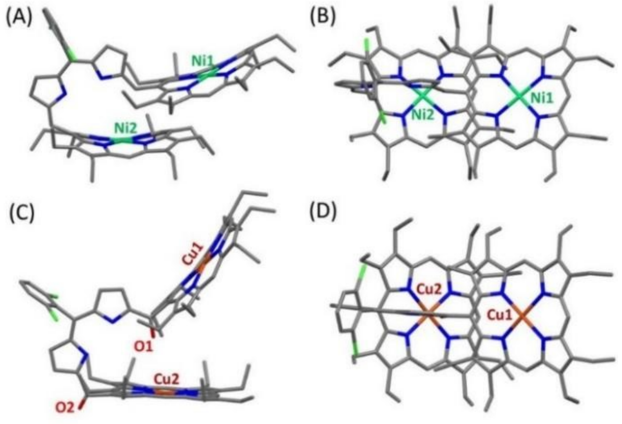

Figure 1. Molecular structures (at 100 K) with two perspective views of **3**•Ni [A, side view and B, top view] and **4**•Cu [C, side view and D, top view] (H atoms and solvent molecules have been omitted for clarity). The atom numbering scheme is displayed in Figure S8.

View Article Online
DOI: 10.1039/D5QI01135G

dipyrromethene bridge, which is placed nearly orthogonal to the porphyrin planes with significant alteration in the bond lengths and angles (Table 1) to make a π-conjugated cofacially sloping structural scaffold, as reflected in the appearance of an intense low-energy band in the UV–visible spectrum (*vide infra*). Each porphyrin macrocycle is also distorted, with a saddle-shape distortion observed in **3**•Ni. Still, the extent of the distortion is less compared to the fully π-conjugated structural motif in **2**•Ni (Table 1). In addition, the Ni•••Ni and Cu•••Cu non-bonding distances are similar (7.41 Å) in both **3**•Ni and **3**•Cu.[14b]

It is interesting to see the drastic structural changes from the π-conjugated curved structure of **3**•Ni to a contorted structure of **4**•Cu, as shown in Figure 1. Two sets of **4**•Cu crystals were grown using two different solvent combinations. One molecule of dichloromethane was present in one of the crystal lattices, while one molecule of *n*-hexane was present in the other. However, the gross structure and geometrical parameters remain very similar in both cases, although unit cells are completely different, along with their solvent of crystallization. The presence of two carbonyl groups at the methine position of the dipyrrin bridge in **4**•Cu forces the porphyrin rings to move away from each other. This has increased the dihedral angle between them, from 20.42° (of **3**•Ni) to 57.0° (of **4**•Cu·C_6H_{14}), and also has increased the Cu•••Cu nonbonding distance from 7.41 Å to 8.79 Å. The average Cu–Np distances in the two porphyrin cores are 1.995(6) Å and 1.999(7) Å, respectively, slightly shorter than **3**•Cu. The bridging C20–C37 and C37–C38 distances are 1.517(9) Å and 1.456(9) Å, respectively, and the bridging angle C20–C37–C38 drastically changes to 116.3(6)°, giving more contortion to the structure. Also, from the crystal structure, it was found that one of the macrocycles opens the cavity from 1.0 nm in **3**•Ni to 1.3 nm in **4**•Cu, and the carbonyl oxygen is directed toward Cu(II) at a distance of 3.78 Å from another porphyrin ring, thus increasing the dihedral angle to 57.0°. The electron-withdrawing nature of the -C=O group and its π-acceptor ability makes electronic communication between the two porphyrin macrocycles possible through the bridge, which is also reflected in the UV-visible spectrum (*vide infra*).

UV-vis-NIR spectroscopy

The absorption spectrum of **1**•Cu in CH_2Cl_2 exhibits a sharp Soret band at 408 nm and two Q-bands at 535 and 568 nm.[14a] Addition of the solution of DDQ in acetonitrile up to two equivalents to the unconjugated complex **1**•Cu in CH_2Cl_2 leads to the formation of **3**•Cu, which displays a blue-shifted sharp Soret band at 402 nm along with an intense Q-band at 561 nm and a broad NIR band at 846 nm (Figures 2 and S9). The spectral features are associated with the formation of a π-conjugated cofacially-sloping structural motif for **3**•Cu. The decrease in intensity of the Q-band and low-energy band in the NIR region of **3**•Cu prior to **2**•Cu could be associated with a drastic change in the shape of the molecule from linear to cofacially sloping. Compared to **2**•Cu, the low-energy NIR band in **3**•Cu is slightly blue-shifted, which indicates a lowering of the conjugation in the complex via the bridge. Similar spectral features have also been observed in **3**•Ni (Figures 2 and S9). The extent of conjugation is thus dependent on the shape of the molecule: a linear structure has better π-conjugation than a curved one.

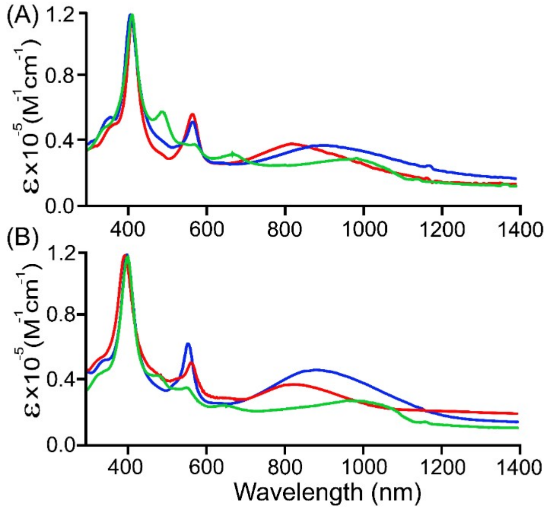

Figure 2. UV-vis-NIR absorption (in CH_2Cl_2 at 295 K) spectra of (A) **2**•Cu (blue line), **3**•Cu (red line), and **4**•Cu (green line), and (B) **2**•Ni (blue line), **3**•Ni (red line), and **4**•Ni (green line).

Complex **4**•Cu, however, exhibits a sharp Soret band at 405 nm and three Q-bands at 475, 560, and 640 nm, along with a low-intense and broad NIR band at 994 nm. Similar spectral features have also been observed for **4**•Ni; the Soret and Q-bands display a slight blueshift, while the low-energy band displays a red-shift with a slight increase in intensity compared to **4**•Cu. Notably, the addition of carbonyl moiety at the methine bridge in **4**•M resulted in more red-shifted absorption spectra into the NIR region (Figures 2 and S9) that might be due to the non-covalent interaction of O atom to Cu (Cu•••O = 3.77Å), as also supported by atoms in molecules (AIM) analysis (*vide infra*).

The time-dependent density functional theory (TD-DFT) calculations effectively correlate with the experimental spectra for all the neutral complexes. In **4**•Cu, a low energy NIR band observed at 994 nm corresponds to the porphyrinic HOMO to the dipyrrinic LUMO (f = 0.0560) with an appreciable electronic amplitude on the bridging group (Figure S10). Similarly, the NIR band of **4**•Ni observed at 1018 nm can be related to the charge transfer nature with the HOMO to dipyrrinic LUMO transition (f = 0.0612) (Figure S11). Interestingly, such a distinctive absorption band was not observed in the unconjugated complex **1**•M (Scheme 1). Compared to that of **2**•M and **3**•M, the low energy band of **4**•M is more red-shifted, which is consistent with their HOMO–LUMO energy gaps calculated by DFT calculation (*vide infra*).

^{1}H NMR Spectroscopy

The molecular shapes of **2**•Ni, **3**•Ni, and **4**•Ni are reflected in the ^{1}H NMR spectra (Figure 3). The resonances related to the DPM bridge show substantial changes in the oxidised complex in **2**•Ni and **3**•Ni due to a variation in the molecular shape, which further changes in **4**•Ni. The advent of two singlets in

View Article Online
DOI: 10.1039/D5QI01135C

2•Ni and **3**•Ni for the methine protons of the bridge further confirm oxidation of the bridge, which produces extensive π-conjugation in Ni(II) porphyrin rings. The absence of the signals of methine protons (Figure 3C) indicates the formation of the carbonyl group in **4**•Ni. Due to the change in the shape of the molecule to **4**•Ni, six meso signals with different patterns than **2**•Ni and **3**•Ni are observed at δ = 10.11, 9.60, 9.75, 9.59, and 9.22 (for two meso protons) ppm, which suggests the retention of an unsymmetrical nature and increased contortion of the two porphyrin rings. The resonances related to the bridging moiety display significant changes due to oxidation and generation of the carbonyl group. The appearance of four resonances for bridging β-pyrrolic protons at δ = 5.52, 5.28, 5.09, and 4.82 ppm are found in a narrow range compared to **2**•Ni and **3**•Ni due to changes in the shape of the molecule. The presence of one –NH proton at δ = 5.33 ppm again indicates the inequivalent nature of two pyrrole rings in the DPM spacer. The ^{1}H NMR spectra of [**3**•Ni]$^{2+}$ and [**4**•Ni]$^{2+}$ complexes are too broad to be informative because of their paramagnetic nature (*vide infra*).

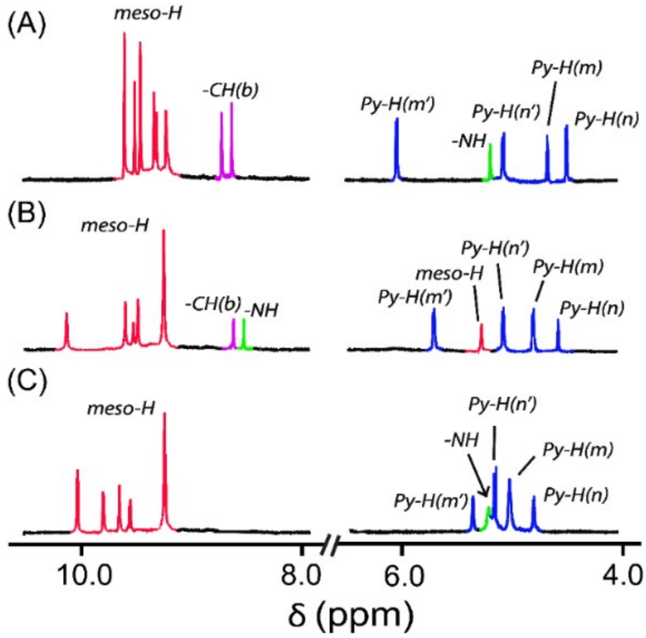

Figure 3. ^{1}H NMR (in $CDCl_3$ at 295 K) spectra of (A) **2**•Ni, (B) **3**•Ni, and (C) **4**•Ni. The numbering scheme used for the ^{1}H NMR assignment is given in Figure S15.

The aromatic behavior of the Ni complexes (i.e., **2**•Ni, **3**•Ni, and **4**•Ni) supported by their distinct 18π-aromaticity based on the negative value of NICS(0)[16a] (NICS = nucleus-independent chemical shifts) at the inner porphyrin core and the observation of the clockwise ring currents in the AICD[16b] plots (AICD = anisotropy of the induced current density) (Figures S12 and S13). Due to the conformational difference among the complexes, the extent of the aromaticity for the **2**•Ni is slightly smaller than those of **3**•Ni and **4**•Ni in terms of NICS values. Consistently, the localized orbital locator (LOL)-π–isosurface map of **2**•Ni revealed a well-defined macrocyclic delocalization channel of the π-electrons through the dipyrrin moiety (Figure S14).[16c] In contrast, the isosurface for **3**•Ni and **4**•Ni is partially disconnected between the meso carbons and dipyrrin moieties due to the large dihedral angles (Figure S14).

Mechanistic Investigation for Formation of 4•M

To gain insights regarding the unusual transformation from **1**•M to **4**•M, we have monitored the progress of the reaction over time using the ESI-MS technique. A possible reaction mechanism is as follows (Figure S1). Initially, DDQ partially oxidises the DPM spacer due to its inherent redox-active nature and loses one of the methine protons to form a carbocation, which thereby facilitates the electrophilic attack of water oxygen to produce a carbonyl group (intermediate **I**-1) as inferred from ESI-MS spectral analysis. During analysis of the crude reaction mixture, m/z = 1507.5668 and 1517.5608 for intermediate **I**-1 of **4**•M were observed in the case of Ni dimer and Cu dimer, respectively (Figures S2 and S3). The intermediate **I**-1 propels the reaction forward by forming another carbocation, which undergoes a series of spontaneous electronic and structural changes in the presence of moisture, resulting in the formation of **4**•M. To confirm the origin of the two carbonyl groups in **4**•M, the ^{18}O labelling experiment using $H_2{}^{18}O$ in the reaction mixture was analysed using ESI mass spectrometry. The molecular ion peak corresponding to m/z = 1536.5873 ion shows that the O-atom introduced in both carbonyls originated from water (Figure S4).

Electrochemical studies

Electrochemical studies of the complexes **3**•Cu, **3**•Ni, **4**•Cu, and **4**•Ni were done using cyclic voltammetry (CV) and differential pulse voltammetry (DPV) at 295 K in dry CH_2Cl_2 containing 0.1 M tetrabutylammonium hexafluorophosphate (TBAH) as a supporting electrolyte under a nitrogen atmosphere (Figure 4). Table 2 shows the comparison of the electrochemical data of the complexes along with **2**•M reported earlier.[14a] The complexes display four successive irreversible oxidative responses with decreased potentials as compared to their unconjugated precursor **1**•M,[14a] which suggests a strong intra-molecular coupling between two metalloporphyrins in the molecules. The oxidative waves of **3**•Cu and **3**•Ni have slightly higher potential than those of **2**•Cu and **2**•Ni. Interestingly, this potential further rises slightly in **4**•Cu and **4**•Ni as compared to **3**•Cu and **3**•Ni due to increased contortion via the generation of the carbonyl group in the redox-active bridge. Moreover, a difference of more than 220 mV between first and second oxidations in these complexes **3**•Cu, **3**•Ni, **4**•Cu, and **4**•Ni also corroborates the occurrence of strong through-bond intra-macrocyclic interactions. In the case of **4**•M, a π*-orbital of the carbonyl group effectively mediates the bonding interaction between a porphyrin ring and DPM spacer, resulting in lowering

View Article Online
DOI: 10.1039/D5QI01135C

Table 2. Selected spectral and electrochemical data at 295 K in CH_2Cl_2.

Complex	UV-vis-NIR Spectral Data (nm)		Electrochemical Data (V)[a,b]				Ref
	Soret band	Q bands	$E^{1/2}$ (ox1)	$E^{1/2}$ (ox2)	$E^{1/2}$ (ox3)	$E^{1/2}$ (ox4)	
2•Ni	402	557, 895	0.56	0.82	1.18	1.52	14a
3•Ni	400	563, 866	0.58	0.81	1.20	1.53	This work
4•Ni	403	471, 554, 635, 1018	0.61	0.85	1.23	1.55	This work
2•Cu	401	557, 875	0.54	0.80	1.20	1.51	14a
3•Cu	402	561, 846	0.56	0.84	1.17	1.50	This work
4•Cu	405	475, 560, 640, 994	0.63	0.86	1.25	1.58	This work

[a]The reference electrode was Ag/AgCl. [b]Potential obtained from DPV (scan rate 100 mV s^{-1} with 0.1 M TBAH as the supporting electrolyte).

of the HOMO−LUMO gap from **3**•M by stabilizing the LUMOs (*vide infra*). These results suggest that the carbonyl group acts as a good π-mediator[17] between the porphyrin ring and the DPM spacer, thus favouring π-communication throughout, as observed in its red-shifted UV–vis–NIR spectra.

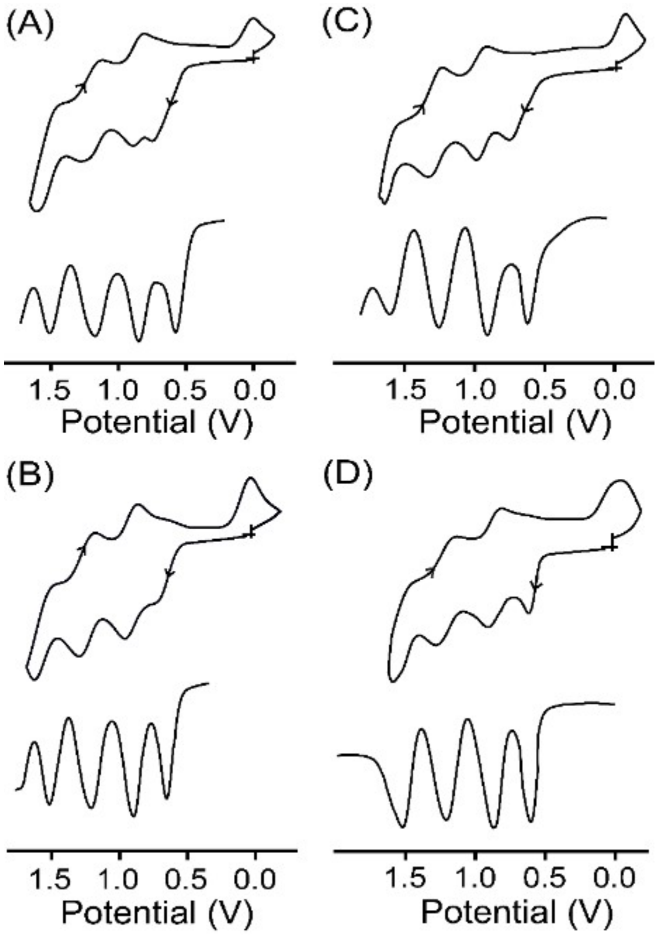

Figure 4. Cyclic voltammograms and differential pulse voltammograms (Oxidation only) of (A) **3**•Cu, (B) **3**•Ni, (C) **4**•Cu, and (D) **4**•Ni determined at 295 K in dry CH_2Cl_2 (scan rate 100 mV s^{-1}) with 0.1 M TBAH as the supporting electrolyte and Ag/AgCl as the reference electrode.

Chemical oxidation of metal complexes

We have previously reported the successful characterization of the oxidized complexes, [**2**•M]SbF_6 or [**2**•M]$^+$ and [**2**•M]$(SbF_6)_2$ or [**2**•M]$^{2+}$.[14a] To gain insight into the reactivities dependent on the molecular structure in these porphyrin arrays, we explored stepwise oxidative reactivities of **3**•M and **4**•M using $AgSbF_6$ as an oxidising agent, Scheme 2. The ESI-MS spectra display intense molecular ion peaks at m/z = 751.2863 for [**3**•Cu]$^{2+}$, and for [**3**•Ni]$^{2+}$ m/z = 746.7892, the experimental isotopic distribution pattern matches precisely with the theoretical one (Figures S19 and S20). The ESI-MS spectra display intense molecular ion peaks at m/z = 766.2931 for [**4**•Cu]$^{2+}$ and m/z = 761.2965 for [**4**•Ni]$^{2+}$, with overlapping experimental and theoretical isotopic distribution patterns (Figures S23 and S24). The resulting π-cation radicals are remarkably stable and can be kept in solid for months under ambient conditions due to their thermodynamically stabilized π-scaffolds.

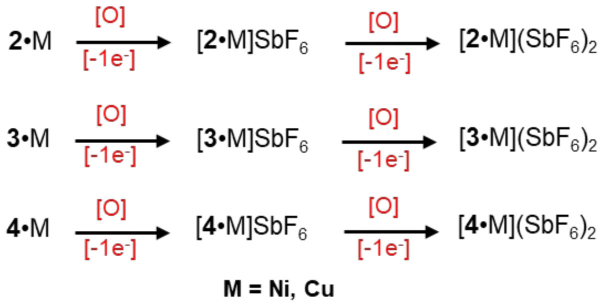

Scheme 2. Synthetic outline of the oxidized complexes and their abbreviations. [O]: $AgSbF_6$.

Oxidations of **3**•M and **4**•M were performed using a chemical oxidant $AgSbF_6$ at 295 K in a stepwise manner and were monitored by UV-vis-NIR absorption spectroscopy. Complex **3**•Cu in CH_2Cl_2 exhibits an intense Soret band at 402 nm, one Q-band at 563 nm, and a low-energy band at 846 (ε, 2.8 × 104 M^{-1} cm^{-1}) nm. Upon gradual addition of one equivalent of $AgSbF_6$ solution in acetonitrile to the CH_2Cl_2 solution of **3**•Cu, the intensity of the Soret band decreases steadily along with a modest red-shift (from 402 to 404 nm). In contrast, the intensity of the Q-band at 561 nm decreases along with the generation of the three new Q-bands at 486, 564, and 680 nm (Figure S16). In addition, an intense NIR absorption band has appeared at 1125 nm with a molar extinction coefficient of ε = 4.8 × 104 M^{-1} cm^{-1} and is diagnostic of the intra-valence charge transfer (IVCT).[18,19] The appearance of such an intense NIR band is due to the strong charge/radical resonance phenomena over the entire π-conjugated framework of the mixed-valence π-cation radical dimer, [**3**•Cu]$^+$. A similar spectral pattern has also been displayed by the one-electron oxidised complex [**3**•Ni]$^+$, leading to three new Q-bands and one strong NIR band at 1095 nm with a molar extinction coefficient of ε = 5.5 × 10^4 M^{-1} cm^{-1} (Figure S17). However, the intensity of the NIR band of [**3**•Cu]$^+$ is slightly lower than that of [**3**•Ni]$^+$, which is presumably due to the more vital electronic interaction between the unpaired spin of the Cu(II) and that of the porphyrin π-cation radical. Prior to linear conjugated [**2**•M]$^+$, the intensity of the NIR bands is low in the case of curved [**3**•M]$^+$, which is probably due to the changes in the molecular shapes from being linear to cofacially sloping with the large dihedral angles (Figures 5, 6, and S18).

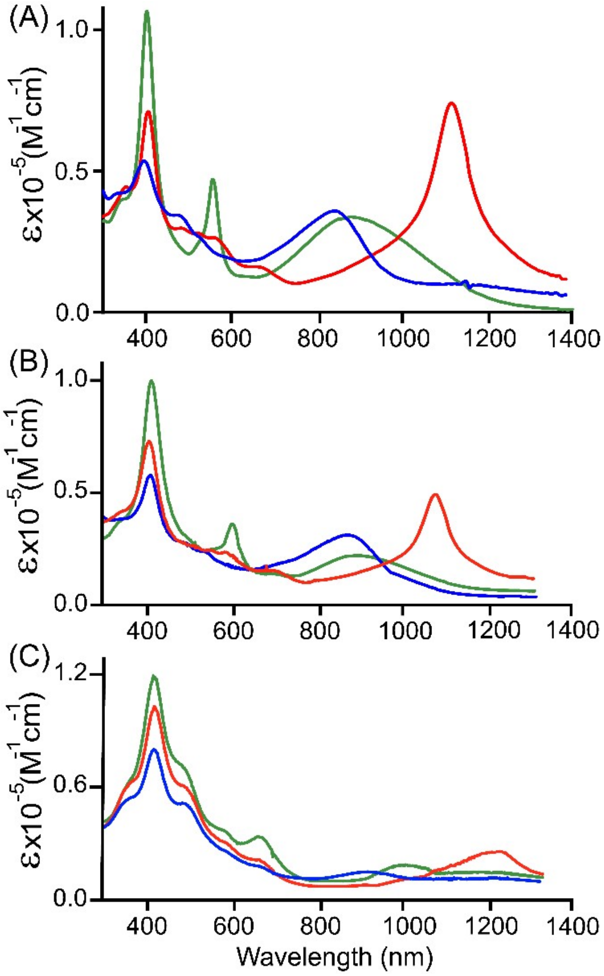

Figure 5. UV-vis-NIR (in CH$_2$Cl$_2$ at 295 K) spectra of (A) **2**•Ni (green line),[14a] [**2**•Ni]SbF$_6$ (red line), and [**2**•Ni](SbF$_6$)$_2$ (blue line); (B) **3**•Ni (green line),[14b] [**3**•Ni]SbF$_6$ (red line), and [**3**•Ni](SbF$_6$)$_2$ (blue line); (C) **4**•Ni (green line), [**4**•Ni]SbF$_6$ (red line), and [**4**•Ni](SbF$_6$)$_2$ (blue line).

With the further addition of the CH$_3$CN solution of AgSbF$_6$, the Soret band intensity at 404 nm slowly decreased again, along with a slight redshift from 404 to 406 nm. Moreover, in [**3**•Cu]$^+$, the Q-band observed at 486 nm increases in intensity while the band at 563 nm completely disappears. Interestingly, the strong NIR band at 1125 nm dissipates again, while a new band appears at 668 nm with a molar extinction coefficient of ε = 3.1 × 10^4 M^{-1} cm^{-1} (Figure S17). These spectral changes correspond to the formation of a dication diradical complex [**3**•Cu]$^{2+}$, which is relatively stable and isolated in the solid state. In the case of [**3**•Ni]$^{2+}$, the spectral pattern is, however, slightly different with the formation of two Q-bands at 479 and 522 nm, with dissipation and the formation of strong NIR bands at 1095 and 855 nm, respectively (Figure S18). Indeed, such a drastic change in the intensity of NIR bands between two isostructural complexes, [**3**•Cu]$^+$ and [**3**•Ni]$^+$, also reflects the effects of metal ions. Similarly, the UV-vis-NIR spectral changes were observed in the 1e$^-$ and 2e$^-$ oxidised complexes of isoelectronic species while moving from [**2**•M]$^{n+}$ to [**3**•M]$^{n+}$ (n = 1 or 2), which corresponds to changes in their molecular shape (Figures 5, 6, and S18).

The UV-vis-NIR spectral features of **4**•M after stepwise oxidation are also characteristic because of the presence of carbonyl groups at the methine positions in the redox-active DPM spacer. Upon gradual addition of one equivalent of AgSbF$_6$ acetonitrile solution to the CH$_2$Cl$_2$ solution of **4**•Cu, the intensity of the Soret band at 405 nm decreases steadily with a small blue-shift of 3 nm along with the formation of a small hump at 357 nm, which can be attributed to charge transfer from bridging oxygen and Cu(II) as they approach closer after 1e$^-$ oxidation. The appearance of the broad NIR-bands around 1075 nm (ε, 2.92 × 10^4 M^{-1} cm^{-1}) of the oxidised species indicates the formation of [**4**•Cu]$^+$. On further addition of AgSbF$_6$ solution, the Soret band intensity at 405 nm slowly decreases again along with blue-shift, and an increase in the intensity of hump at 357 nm further intensifies the charge transfer band. Moreover, the band at 480 and 645 nm decreases drastically, along with the decrease of the NIR band and the subsequent emergence of a new broadened band around 785 nm (ε, 3.2 × 10^4 M^{-1} cm^{-1}). These spectral changes correspond to the formation of a dication diradical complex [**4**•Cu]$^{2+}$ (Figure S21). Similar spectral behavior was observed in their corresponding nickel(II) complexes (Figure S22). However, compared to the 1e$^-$- and 2e$^-$-oxidised species of **2**•M and **3**•M, the intensities of low energy bands in **4**•M significantly decreased, consistent with the TD-DFT simulated spectra (*vide infra*).

Upon comparing the UV-vis-NIR spectra of each oxidised species, it has been observed that 1e$^-$ and 2e$^-$ oxidised species of **2**•M exhibit more intense NIR absorption bands than those of **3**•M and **4**•M in their respective metal complexes. As reflected by the intensity of NIR bands, the strength of conjugation in the respective metal complex could follow the order [**2**•M]$^{n+}$ >

View Article Online
DOI: 10.1039/D5QI01135C

Table 3. Experimental and DFT computed exchange-coupling constants (*J*'s) in the complexes.

Exchange type	[**2**•Cu](SbF$_6$)$_2$		[**2**•Ni](SbF$_6$)$_2$		[**3**•Cu](SbF$_6$)$_2$		[**3**•Ni](SbF$_6$)$_2$		[**4**•Cu](SbF$_6$)$_2$		[**4**•Ni](SbF$_6$)$_2$	
	J_{DFT} (cm^{-1})	J_{sim} (cm^{-1})	J_{DFT} (cm^{-1})	J_{sim} (cm^{-1})	J_{DFT} (cm^{-1})	J_{sim} (cm^{-1})	J_{DFT} (cm^{-1})	J_{sim} (cm^{-1})	J_{DFT} (cm^{-1})	J_{sim} (cm^{-1})	J_{DFT} (cm^{-1})	J_{sim} (cm^{-1})
$J_{Cu\text{-}Cu}$	1.5	1.3	–	–	1.8	2.3	–	–	2.1	2.6	–	–
$J_{Cu\text{-}r}$	−113.0	−92.6	–	–	−48.0	−68.3	–	–	−53.0	−79.1	–	–
$J_{r\text{-}r}$	−24.4	−25.3	-	−25.7	−18.5	−21.1	−19.3	−21.8	−10.2	−17.6	−11.0	−17.5

[**3**•M]$^{n+}$ > [**4**•M]$^{n+}$ (n = 1 or 2), thus highlighting the importance of the molecular shapes along with the conjugation pathway (Figures 5 and 6). Similar spectral observations were also made in isostructural complexes upon changing only the metal from nickel to copper, where molar extinction coefficients and intensity of NIR bands in the case of oxidised nickel species dominate over copper complexes, signifying the role of metal ions as well (Figure 6).

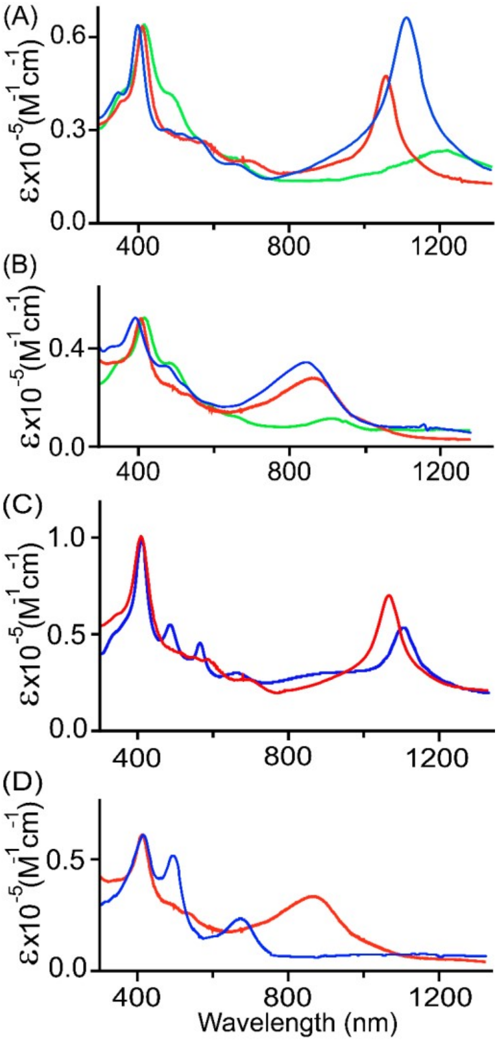

Figure 6. UV-vis-NIR (in CH$_2$Cl$_2$ at 295 K) spectra of (A) [**2**•Ni]SbF$_6$ (blue line),[14a] [**3**•Ni]SbF$_6$ (red line), and [**4**•Ni]SbF$_6$ (green line); (B) [**2**•Ni](SbF$_6$)$_2$ (blue line),[14a] [**3**•Ni](SbF$_6$)$_2$ (red line), and [**4**•Ni](SbF$_6$)$_2$ (green line); (C) [**3**•Cu]SbF$_6$ (blue line) and [**3**•Ni]SbF$_6$ (red line) and (D) [**3**•Cu](SbF$_6$)$_2$ (blue line) and [**3**•Ni](SbF$_6$)$_2$ (red line).

Magnetic susceptibility measurements

The magnetic susceptibility measurements of 2e$^-$-oxidized complexes [**3**•M](SbF$_6$)$_2$ and [**4**•M](SbF$_6$)$_2$ were carried out under a 0.1 T magnetic field over the temperature range of 5 to 300 K. Temperature-dependent magnetization data for all complexes are presented in Figure 7. At room temperature, the $\chi_M T$ values of [**3**•Cu](SbF$_6$)$_2$, [**3**•Ni](SbF$_6$)$_2$, [**4**•Cu](SbF$_6$)$_2$, and [**4**•Ni](SbF$_6$)$_2$ were found to be 1.16, 0.71, 1.11, and 0.71 cm^3 K mol^{-1}, respectively. These values differ significantly from the expected theoretical value of approximately 3.0, 1.0, 3.0, and 1.0 cm^3 K mol^{-1}, respectively, for uncoupled systems. This is attributed to the strong antiferromagnetic coupling that remains effective even at room temperature. As the temperature decreases, in Cu-complexes, the $\chi_M T$ values decrease gradually to 100 K, and thereafter, they decrease sharply, suggesting various competing exchanges that are operational in these complexes. In Ni-complexes, the $\chi_M T$ value decreases rapidly as temperature decreases due to the increasing population of antiferromagnetic singlet state (S = 0) due to radical-radical exchange between two porphyrins. The susceptibility data indicate dominant antiferromagnetic coupling in all four complexes, as the room temperature susceptibility is less than expected for two *S* = 1/2 Cu(II) and two *S* = 1/2 radical centres. One magnetic exchange ($J_{r\text{-}r}$) in the Ni-complex and three magnetic exchanges ($J_{Cu\text{-}Cu}$, $J_{Cu\text{-}r}$, and $J_{r\text{-}r}$) in the Cu-complexes are possible. The following exchange Hamiltonians (eq. (i) for Ni complexes and eq. (ii) for Cu complexes) have been used to compute the several *J's*:

$$\hat{H} = -2J_{r-r}S_{Ni^1_{rad}}S_{Ni^2_{rad}} \qquad \textbf{(i)}$$

$$\hat{H} = -2\left[J_{Cu-Cu}S_{Cu1}S_{Cu2} + J_{Cu-r}\left(S_{Cu1}S_{Cu^1_{rad}} + S_{Cu2}S_{Cu^2_{rad}}\right) + J_{r-r}S_{Cu^1_{rad}}S_{Cu^2_{rad}}\right] \qquad \textbf{(ii)}$$

As fitting the magnetic susceptibility with different exchanges, particularly in the [**4**•Cu](SbF$_6$)$_2$, can lead to an over-parameterization problem, we have performed broken symmetry density functional theory (BS-DFT) calculations using Gaussian 16 suite[20] employing unrestricted B3LYP functional, def2TZVP basis set for Cu/Ni and def2SVP basis set for other

View Article Online
DOI: 10.1039/D5QI01135C

atoms (see computational details in ESI for more information). This methodology has a proven track record of yielding good numerical estimates of *J* values. The DFT-optimised structures are in close agreement with the experimental X-ray structures (*vide supra*). The BS-DFT calculation estimates the $J_{Cu\text{-}Cu}$, $J_{Cu\text{-}r}$, and $J_{r\text{-}r}$ values of 1.8 cm^{-1}, –48.0 cm^{-1}, and –18.5 cm^{-1}, respectively, for [**3**•Cu](SbF6)2 and 2.1 cm^{-1}, –53.0 cm^{-1}, and –10.2 cm^{-1} for [**4**•Cu](SbF$_6$)$_2$.

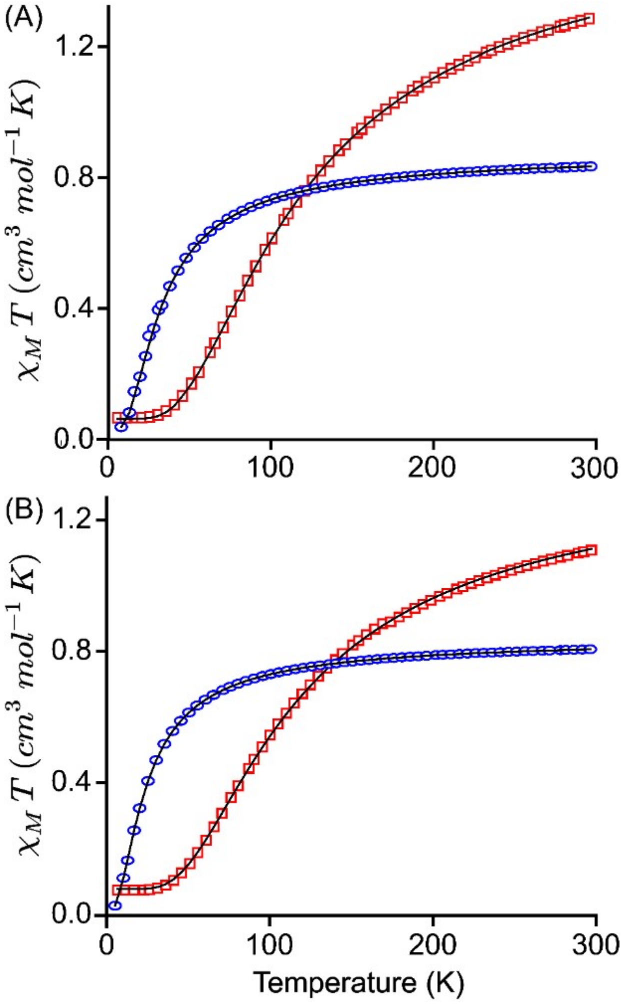

Figure 7. $X_M T$ versus *T* plots for (A) [**3**•Cu](SbF$_6$)$_2$ (blue trace) and [**3**•Ni](SbF$_6$)$_2$ (red trace) and (B) [**4**•Cu](SbF$_6$)$_2$ (blue trace) and [**4**•Ni](SbF$_6$)$_2$ (red trace). The solid black lines represent the best fit using PHI suite.

Magnetic exchange coupling computed from DFT calculation has been used as an initial guess to simulate the susceptibility curve (χ_MT vs. T) for complexes using the PHI[21] software. The best fit obtained from the PHI simulation is given in Figure 7, and the observed J values are listed in Table 3. The fitted curve suggests that, in general, the exchange-coupling estimated from the DFT calculation is overestimated, which is consistent with our previously reported systems.[22] From the PHI simulations, $J_{Cu\text{-}Cu}$ values obtained are 1.3 cm^{-1}, 2.3 cm^{-1} and 2.6 cm^{-1}, respectively, for [**2**•Cu](SbF$_6$)$_2$, [**3**•Cu](SbF$_6$)$_2$, and [**4**•Cu](SbF$_6$)$_2$ while $J_{Cu\text{-}r}$ values are –92.6 cm^{-1}, –68.3 cm^{-1} and –79.1 cm^{-1}. Also, the simulated $J_{r\text{-}r}$ was found to be –25.3 cm^{-1}, –25.7 cm^{-1}, –21.1 cm^{-1}, –21.8 cm^{-1}, –17.6 cm^{-1} and –17.5 cm^{-1}, respectively, for [**2**•Cu](SbF$_6$)$_2$, [**2**•Ni](SbF$_6$)$_2$, [**3**•Cu](SbF$_6$)$_2$, [**3**•Ni](SbF$_6$)$_2$, [**4**•Cu](SbF$_6$)$_2$ and [**4**•Ni](SbF$_6$)$_2$. These PHI-simulated *J*'s (experimental values) agree well with the DFT-computed values.

The $J_{Cu\text{-}Cu}$ magnetic exchange is found to be weakly ferromagnetic, and this is due to the very large Cu•••Cu distance (15.5 Å), which agrees well with the previous reports[14a] in similar systems, where the Cu•••Cu distance of around 10–13 Å yields the ferromagnetic interaction of the order of 1–10^{-4} cm^{-1}. The $J_{Cu\text{-}Cu}$ exchange increases from 1.3 cm^{-1} ([**2**•Cu](SbF$_6$)$_2$) to 2.3 cm^{-1} ([**3**•Cu](SbF$_6$)$_2$) followed by 2.6 cm^{-1} ([**4**•Cu](SbF$_6$)$_2$) and this is due to decrease in the Cu•••Cu distance, where it changes from 15.5 Å ([**2**•Cu](SbF$_6$)$_2$) to 6.2 Å ([**3**•Cu](SbF$_6$)$_2$) followed by 6.7 Å ([**4**•Cu](SbF$_6$)$_2$). In [**4**•Cu](SbF$_6$)$_2$, the metal-metal distance increases by 0.5 Å, the increase in $J_{Cu\text{-}Cu}$ could be attributed to the interaction between the Cu centre and oxygen atom (Cu•••O = 2.5 Å) as suggested by the presence of bond critical point computed from the atoms in the molecule (AIM) analysis (Figure S25). The $J_{Cu\text{-}r}$ exchange was calculated using the model system (Figures S26 and S27), where the significant metal-radical exchange was estimated due to the strong overlap between the singly occupied $d_{x^2-y^2}$ orbital of Cu and porphyrin π-singly occupied molecular orbital (SOMO, see Figure S27). The $J_{r\text{-}r}$ exchange in the [**3**•Cu](SbF$_6$)$_2$ and [**4**•Cu](SbF$_6$)$_2$ was computed to be –21.1 cm^{-1} and –17.6 cm^{-1}, respectively (Table 3), which is relatively weaker than an antiferromagnetic exchange of –25.3 cm^{-1} present in [**2**•Cu](SbF$_6$)$_2$. A similar trend was observed on going from [**2**•Ni](SbF$_6$)$_2$ (–25.7 cm^{-1}) to [**3**•Ni](SbF$_6$)$_2$ (–21.8 cm^{-1}), followed by [**4**•Ni](SbF$_6$)$_2$ (–17.5 cm^{-1}), respectively. It is important to note that our attempts to compute DFT-based *J* values for [**2**•Ni](SbF$_6$)$_2$, were unsuccessful due to convergence issues associated with the targeted electronic configurations.

As observed from Table 3, $J_{r\text{-}r}$ exchange decreases on going from [**2**•M](SbF$_6$)$_2$ to [**3**•M](SbF$_6$)$_2$ followed by [**4**•M](SbF$_6$)$_2$. This trend of decreasing exchange-coupling constant suggests that the extent of kinetic exchange of the radical spin (delocalization) between the intra-porphyrins decreases, which implies that electronic communication through conjugation decreases. The decreased conjugation on going from linear to cofacially slopping followed by clamshell is also supported by the increased HOMO–LUMO gap and (LOL)-π isosurface map (*vide infra*). The [**2**•Cu](SbF$_6$)$_2$, [**3**•Cu](SbF$_6$)$_2$, and [**4**•Cu](SbF$_6$)$_2$ follow the trend for the HOMO–LUMO gap 0.87 eV < 1.04 eV < 2.14 eV while in [**2**•Ni](SbF$_6$)$_2$, [**3**•Ni](SbF$_6$)$_2$ and [**4**•Ni](SbF$_6$)$_2$ have the order 1.36 eV < 1.91 kJ/mol < 2.38 eV.

EPR spectroscopy

The EPR spectral behavior of **3**•Cu and **4**•Cu (Figures 8 and 9) is similar to that displayed by **2**•Cu, reported recently by us.[14a] In unoxidised form, **3**•Cu and **4**•Cu show the signals of mononuclear copper(II) species in the ground doublet state, suggesting that the magnetic interaction between the unpaired

View Article Online
DOI: 10.1039/D5QI01135C

electrons on two Cu(II) ions does not occur through space nor the bridge. The spin Hamiltonian parameters are: $g_{x,y,z}$ = {2.044, 2.044, 2.192}, $A_{x,y,z}$(Cu) = {26.5, 26.5, 201.6} × 10^{-4} cm^{-1}, $A_{x,y,z}$(^{14}N) = {15.5, 15.5, 17.0} × 10^{-4} cm^{-1} for **3**•Cu, and $g_{x,y,z}$ = {2.048, 2.048, 2.193}, $A_{x,y,z}$(Cu) = {24.5, 24.5, 202.8} × 10^{-4} cm^{-1}, $A_{x,y,z}$(^{14}N) = {15.3, 15.3, 15.3} × 10^{-4} cm^{-1} for **4**•Cu (Table 4). The relative values of the hyperfine coupling constants, A_z(Cu) >> A_x(Cu) ~ A_y(Cu) > 0, are compatible with the square planar structure disclosed by X-ray diffraction analysis (Table 1) and a ground state based on Cu d_{x2-y2} orbital.[23] The values of A_z(Cu), in the range (200–210) × 10^{-4} cm^{-1}, agree well with those reported for Cu(II)-porphyrins.[13c,14a,23,24] Similarly, the superhyperfine coupling constant with nitrogen nuclei, A(^{14}N), is comparable to those discussed in literature, between 15.0 × 10^{-4} cm^{-1} and 18.0 × 10^{-4} cm^{-1}.[13c, 14a,24]

Upon the chemical oxidations of **3**•Cu and **4**•Cu the resonances centred around 3040 and 3530 G (denoted by the black squares) attributed to the perpendicular region of a signal belonging to a triplet state (2S + 1 = 3); in addition four of the seven absorptions expected in the parallel region (septet with an intensity ratio 1:2:3:4:3:2:1 [25]) are revealed (they are indicated with the black triangle and the asterisks). The spectrum of [**3**•Cu]$^{2+}$ was simulated with $g_{x,y,z}$ = {2.042, 2.042, 2.380}, $A_{x,y,z}$(Cu) = {10.0, 10.0, 102.0} × 10^{-4} cm^{-1}, D (zero-field splitting) = 218 × 10^{-4} cm^{-1}, E (rhombic parameter) = 72.7 × 10^{-4} cm^{-1} and that of [**4**•Cu]$^{2+}$ with $g_{x,y,z}$ = {2.047, 2.047, 2.378}, $A_{x,y,z}$(Cu) = {10.0, 10.0, 102.0} × 10^{-4} cm^{-1}, D = 220 × 10^{-4} cm^{-1}, E = 73.3 × 10^{-4} cm^{-1} (Table 4); in both cases, the final spectra were obtained summing to the signals of [**3**•Cu]$^{2+}$or [**4**•Cu]$^{2+}$, along with a small proportion of the signal deriving from their respective unoxidised complexes **3**•Cu and **4**•Cu. The value of A_z(Cu) for the septet between 2300 and 3000 G is ca. 102.0 × 10^{-4} cm$^{-1,}$ which is approximately half of that detected for an unoxidised Cu(II) species with the same equatorial coordination;[25] for comparison, A_z for **3**•Cu and **4**•Cu are 201.6 × 10^{-4} cm^{-1} and 202.8 × 10^{-4} cm^{-1}, respectively (Table 4).

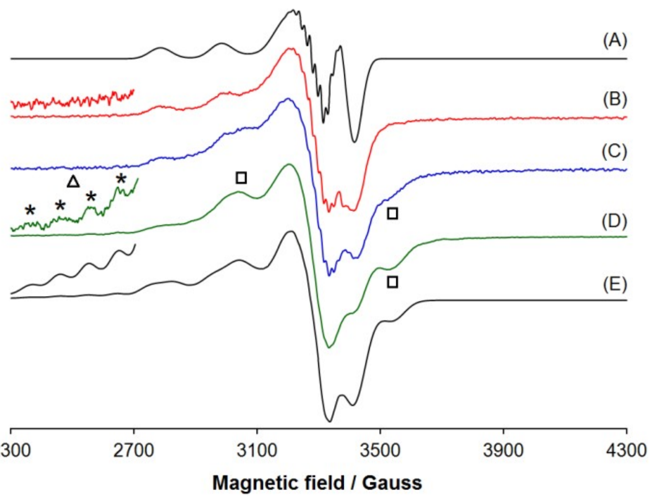

Figure 8 (A) Simulated EPR spectrum of **3**•Cu; (B) experimental EPR spectrum of **3**•Cu (in the CHCl$_3$/toluene mixture at 120 K); (C) experimental EPR spectrum of [**3**•Cu]$^+$ (in the CHCl$_3$/toluene mixture at 120 K); (D) experimental EPR spectrum of [**3**•Cu]$^{2+}$ (in the CHCl$_3$/toluene mixture at 120 K); (E) simulated EPR spectrum of [**3**•Cu]$^{2+}$. The triangles and squares indicate the parallel and perpendicular components of the zero-field splitting tensor D, respectively. In the inset and with the asterisks, the hyperfine resonances due to the coupling between the two unpaired electrons and Cu nuclei are denoted; this region, in the magnetic field range 2300–2715 G, was amplified 20, 12, and 9 times compared to the traces (B), (D), and (E).

Considering that (i) the magnetic susceptibility measurements suggest a strong antiferromagnetic interaction between Cu(II) and porphyrin radical cations, (ii) the absence of a through space coupling Cu(II)···Cu(II) for **3**•Cu and **4**•Cu (see traces B of Figures 8 and 9), and (iii) the positive value of J_{Cu-Cu}, the results of EPR spectroscopy can be explained by assumption that the oxidation of **3**•Cu and **4**•Cu promotes intramolecular electronic communication between the two Cu(II) centres upon conformational changes, as suggested by UV-vis-NIR spectroscopy. This confirms the possibility of a long-range spin communication through a π-conjugated bridge for dinuclear metalloporphyrins.[14a]

The EPR spectra recorded on the 2e$^-$-oxidised species, [**3**•Cu]$^{2+}$ and [**4**•Cu]$^{2+}$ in the solid state (Figure 10) provide new insights; the pattern is attributable to a triplet spin state in both cases. For [**3**•Cu]$^{2+}$ the spin Hamiltonian parameters are $g_{x,y,z}$ = {2.049, 2.049, 2.370}, $A_{x,y,z}$(Cu) = {10.0, 10.0, 101.0} × 10^{-4} cm^{-1}, D = 220 × 10^{-4} cm^{-1}, E = 73.3 × 10^{-4} cm^{-1} and for [**4**•Cu]$^{2+}$ they are $g_{x,y,z}$ = {2.045, 2.045, 2.350}, $A_{x,y,z}$(Cu) = {10.0, 10.0, 103.0} × 10^{-4} cm^{-1}, D = 230 × 10^{-4} cm^{-1}, E = 76.7 × 10^{-4} cm^{-1} (Table 4).

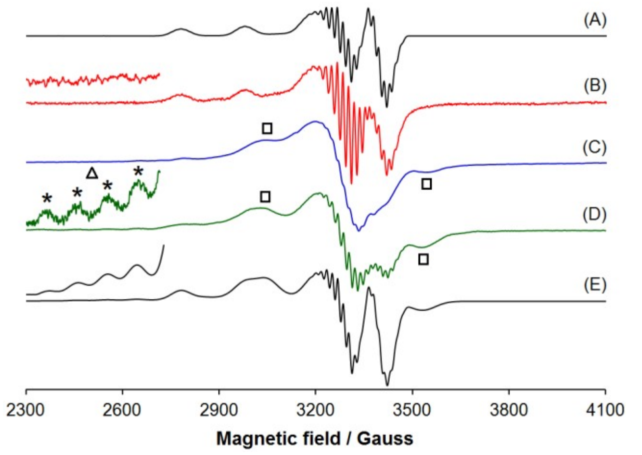

Figure 9. (A) Simulated EPR spectrum of **4**•Cu; (B) experimental EPR spectrum of **4**•Cu (in the CHCl$_3$/toluene mixture at 120 K); (C) experimental EPR spectrum of [**4**•Cu]$^+$ (in the CHCl$_3$/toluene mixture at 120 K); (D) experimental EPR spectrum of [**4**•Cu]$^{2+}$ (in the CHCl$_3$/toluene mixture at 120 K); (E) simulated EPR spectrum of [**4**•Cu]$^{2+}$. The triangle and squares indicate the parallel and perpendicular components of the zero-field splitting tensor D, respectively. In the inset and with the asterisks, the hyperfine resonances due to the coupling between the two unpaired electrons and Cu nuclei are denoted; this region, in the magnetic field range 2300–2715, was amplified 25, 25, and 16 times compared to the traces (B), (D), and (E).

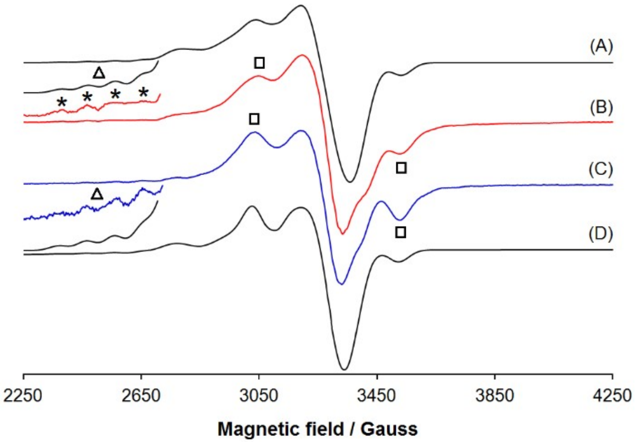

Figure 10. (A) Simulated EPR spectrum of [**3**•Cu]$^{2+}$; (B) experimental EPR spectrum of [**3**•Cu]$^{2+}$ (in the solid state at 120 K); (C) experimental EPR spectrum of [**4**•Cu]$^{2+}$ (in the solid state at 120 K); (D) simulated EPR spectrum of [**4**•Cu]$^{2+}$. The triangles and squares indicate the parallel and perpendicular components of the zero-field splitting tensor *D*, respectively. In the inset and with the asterisks, the hyperfine resonances due to the coupling between the two unpaired electrons and the two Cu nuclei are denoted; this region, in the magnetic field range 2300–2715, between 2300 and 2715 G, was amplified 6, 6, 9, and 8 times compared to the traces (A)-(D).

This confirms that the formation of por$^{+\bullet}$ promotes spin communication for Cu(II) complexes. Moreover, oxidation does not involve the metal centre, and nickel maintains the +2-oxidation state. The magnetic interaction detected for [**3**•Cu]$^{2+}$ and [**4**•Cu]$^{2+}$ in the solid state is different; for example, the zero-field splitting tensor values of *D* are 220 × 10^{-4} cm^{-1} and 230 × 10^{-4} cm^{-1} for [**3**•Cu]$^{2+}$ and [**4**•Cu]$^{2+}$, respectively (Table 4). This suggests, as indicated by other spectroscopic techniques, that the type of chemical bridge and shape of the complex modulate the spin coupling.

The experimental and simulated spectra of [**4**•Cu]$^{2+}$ in the solid state are compared in Figure S28. The composite resonances at the half-field, between 1450 and 1680 G, are typical of molecules in a triplet state and can be attributed to the forbidden transition $\Delta M_S = \pm 2$, observed for many dinuclear Cu(II) complexes, confirming the chemical nature of [**4**•Cu]$^{2+}$.[25] It can also be noted that the intensity ratio between the first four parallel absorptions (region 2300–2715 G) is 1:2:3:4, as predicted for the interaction of two copper(II) ions.[25] Overall, these findings confirm the electronic communication between the two unpaired electrons on the two Cu(II) centres $J_{\text{Cu-Cu}}$ could be attributed to the interaction between the Cu centre and oxygen atom (Cu•••O = 2.5 Å) as suggested by the presence of bond critical point computed from the AIM analysis (Figure S25).

The EPR spectra recorded on **3**•Ni and **4**•Ni and their oxidised derivatives confirmed some of the findings for copper(II) species. The spectra are silent for **3**•Ni and **4**•Ni due to the diamagnetic configuration of square planar d^8 Ni(II) centres. The spectra of [**3**•Ni]$^{2+}$ and [**4**•Ni]$^{2+}$ show the signals of a radical centred at *g* = 2.006 and *g* = 2.005, respectively (Figure S29).

Computational study

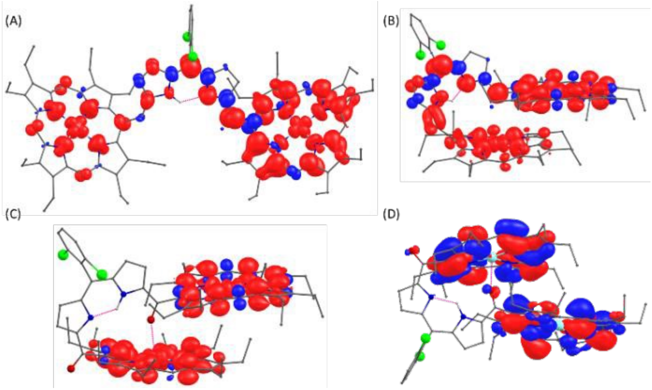

Figure 11. DFT computed spin density distribution throughout the molecule, indicating the extent of conjugation in (A) [**2**•Cu]$^{2+}$, (B) [**3**•Cu]$^{2+}$, and (C) [**4**•Cu]$^{2+}$. (D) Orbital interactions between intra-porphyrins showing electronic communication through Cu•••O interaction. The pink dotted line represents non-covalent interactions. Hydrogen atoms attached to carbons were omitted for clarity.

View Article Online
DOI: 10.1039/D5QI01135C

Table 4. Spin Hamiltonian parameters for **2**•Cu, **3**•Cu, and **4**•Cu and their corresponding 2e⁻-oxidised species [**2**•Cu]$^{2+}$, [**3**•Cu]$^{2+}$, and [**4**•Cu]$^{2+}$.

Complex	g_x	g_y	g_z	A_x(Cu)[a]	A_y(Cu)[a]	A_z(Cu)[a]	A_x(^{14}N)[a]	A_y(^{14}N)[a]	A_z(^{14}N)[a]	D[a]	E[a]	Ref
2•Cu	2.025	2.065	2.188	23.0	25.0	200.0	18.0	18.0	18.0	–	–	14a
3•Cu	2.044	2.044	2.192	26.5	26.5	201.6	15.5	15.5	17.0	–	–	Tw
4•Cu	2.048	2.048	2.193	24.5	24.5	202.8	15.3	15.3	15.3	–	–	Tw
[**2**•Cu](SbF$_6$)$_2$	2.050	2.035	2.368	5.0	10.0	100.0	18.0	18.0	18.0	216.0	72.0	14a
[**3**•Cu](SbF$_6$)$_2$,[b]	2.042	2.042	2.380	10.0	10.0	102.0	15.5	15.5	17.0	216.0	72.0	Tw
[**3**•Cu](SbF$_6$)$_2$,[c]	2.049	2.049	2.370	10.0	10.0	101.0	15.5	15.5	17.0	220.0	73.3	Tw
[**4**•Cu](SbF$_6$)$_2$,[b]	2.047	2.047	2.378	10.0	10.0	102.0	15.3	15.3	15.3	218.0	72.7	Tw
[**4**•Cu](SbF$_6$)$_2$,[c]	2.045	2.045	2.350	10.0	10.0	103.00	15.3	15.3	15.3	230.0	76.7	Tw

[a] Values in 10^{-4} cm^{-1} units. [b] In a mixture of CHCl$_3$/toluene. [c] In the solid state.

The geometry and structural parameters obtained from the DFT calculations agree with the experiment (Figures S30–S33). In **3**•Ni and **4**•Ni, all the electrons are paired and thus produce a closed shell singlet state. The spin density distribution in neutral species **3**•Cu and **4**•Cu (S = 1, triplet state) showed that the spin is mainly found on both the Cu(II) centres with the same phase in the metal d_{x2-y2} orbital (Figures S34 and S35).

However, the spin distribution completely changes after 1e⁻ oxidation in Ni(II) and Cu(II) complexes. In the 1e⁻ oxidised complex [**3**•Ni]$^{+}$ (S = 1/2, doublet state), the spin density is distributed symmetrically on both the porphyrin rings through the DPM bridge with an alternate phase change pattern indicating the effective spin delocalization of π-cation radical on the entire molecule (Figure S36). In contrast, the spin density in [**4**•Ni]$^{+}$ was primarily found on one nickel(II) porphyrin plane, indicating the breaking of the spin delocalization over the bridge due to the carbonyl moiety over the methine bridge as discussed above. In the 1e⁻-oxidised complexes, the doublet state is more stable than the quartet state by 7.90 and 14.12 kcal mol^{-1}, respectively (Figures S34 and S35). There is no change in the spin densities of the copper before and after oxidations; thus, there are no metal-centre oxidations in [**3**•Cu]$^{+}$ and [**4**•Cu]$^{+}$. This agrees well with EPR results.

On this basis, the 2e⁻-oxidised complexes [**3**•Ni]$^{2+}$ and [**4**•Ni]$^{2+}$ have also been optimized in two possible spin multiplicities: an open-shell singlet state, in which two cation radicals endure antiferromagnetic coupling, and a triplet state, where two cation radical spins interact ferromagnetically. The open-shell singlet state was found to be more stable than the triplet state by 8.5 kcal mol^{-1} for [**3**•Ni]$^{2+}$ and by 5.3 kcal mol^{-1} for [**4**•Ni]$^{2+}$ (Figures S36 and S37). In the case of [**4**•Cu]$^{2+}$, three possible spin multiplicities are considered: (i) open-shell singlet state, which accounts for antiferromagnetic interactions between unpaired electrons of Cu(II) and porphyrin π-cation radical spin; (ii) quintet state, which arises due to ferromagnetic coupling between porphyrin π-cation radical and Cu(II) unpaired spins and (iii) triplet state in which two radical spins endure strong antiferromagnetic interaction. The open-shell singlet state has been energetically found to be the most stable in both complexes. Relative energies were found to be in the order: open-shell singlet (0 kcal mol^{-1}) < quintet (5.71 kcal mol^{-1}) < triplet (21.12 kcal mol^{-1}) for [**3**•Cu]$^{2+}$. A similar order was also found in [**4**•Cu]$^{2+}$ (Figures S34 and S35).

The decrease in electronic communication and magnetic exchange coupling constants is also supported by the computed spin density plot, where a fully delocalized spin density is predicted in [**2**•M](SbF$_6$)$_2$ while a distinct localization is determined in [**4**•M](SbF$_6$)$_2$ (Figure 11). The spin density plots display the distribution over the entire molecule with significant contributions on the bridging moiety in the 2e⁻-oxidised complexes of [**2**•M] and [**3**•M]. In contrast, no such spin distribution via the DPM bridge was observed in the case of **4**•M after oxidation. It is important to note that the spin-density plots for the Cu(II) and Ni(II) porphyrin dimers in the neutral, 1e⁻-, and 2e⁻-oxidised states of **2**•M, **3**•M, and **4**•M demonstrate the significance and crucial role of metal ions, bridge and their shape in the intramolecular electronic communication. The overall spectral features of the oxidised species were well-reproduced by the TD-DFT analysis with the UB3LYP method. The characteristic NIR bands at 1075 and 855 nm observed in the 1e⁻- and 2e⁻-oxidised species of **3**•Ni are attributed to the

View Article Online
DOI: 10.1039/D5QI00235C

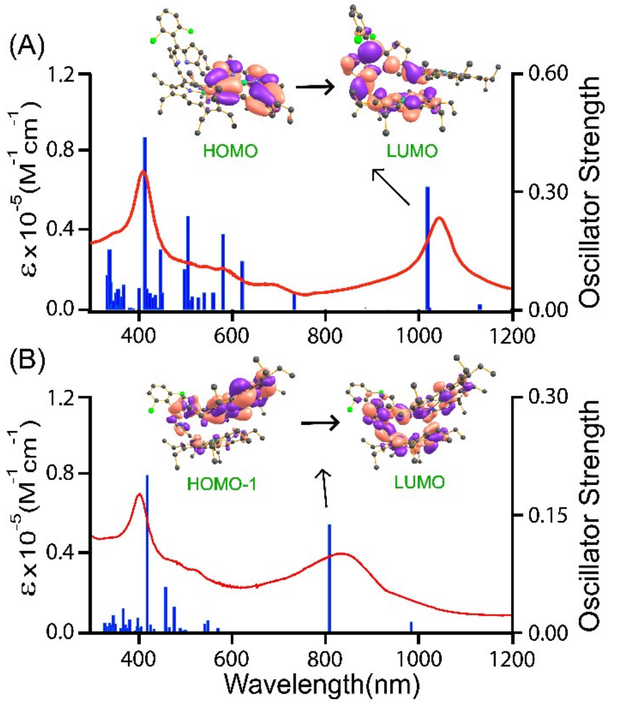

Figure 12. Electronic absorption spectra (curved line, left axis) in CH_2Cl_2 and oscillator strengths (vertical line, right axis) obtained from TD-DFT calculations at the UB3LYP/6-31G**/LANL2DZ level of theory for (A) [**3**•Ni]SbF_6 and (B) [**3**•Ni]$(SbF_6)_2$.

transitions from α-orbitals of HOMO to LUMO (f = 0.3267) and HOMO-1 to LUMO (f = 0.1551), respectively (Figure 12). A similar feature showing strong NIR bands at 1125 and 678 nm for the resulting oxidized species of **3**•Cu, is originated from the transitions from HOMO to LUMO (f = 0.3025) and HOMO to LUMO+2 (f = 0.1135), respectively (Figure S38). This result indicates that the transition behaviors of oxidized **3**•M are both governed by the specific orientation of π-conjugated porphyrin arrays. Furthermore, in the case of **4**•Ni, the 1e$^-$-oxidised NIR band at 1192 nm can be correlated to the transitions from HOMO to LUMO (f = 0.0737), and its 2e$^-$-oxidised band at 912 nm corresponds to HOMO-1 to LUMO (f = 0.0782). Similarly, the 1e$^-$ and 2e$^-$-oxidised species of **4**•Cu at 1075 nm and 785 nm, respectively, correspond to transitions from HOMO to LUMO (f = 0.0687), and HOMO-1 to LUMO (f = 0.0805) (Figures S39 and S40). The above spectral features in the NIR region vary from the corresponding species of **2**•M (M = Ni and Cu), showing the fully delocalized electron density distribution over the porphyrin and DPM bridges originated from the frontier MOs (e.g., HOMO and LUMO) (Figures S41 and S42). The linearly orientated **2**•M may possess electronic structures similar to the oxidised ethynyl-bridged porphyrin dimer, showing NIR absorption with enormous oscillator strengths.[26a] In contrast, the oxidised cofacially bent dimers (i.e., **3**•M and **4**•M) demonstrated the partial/pure charge transfer character upon photoexcitations from the HOMOs to the LUMOs (Figures 12 and S38–S40). The restricted π-electronic communications between the cofacial porphyrin arrays through the dipyrrin moiety in **3**•M and the further disrupted π-conjugation with the

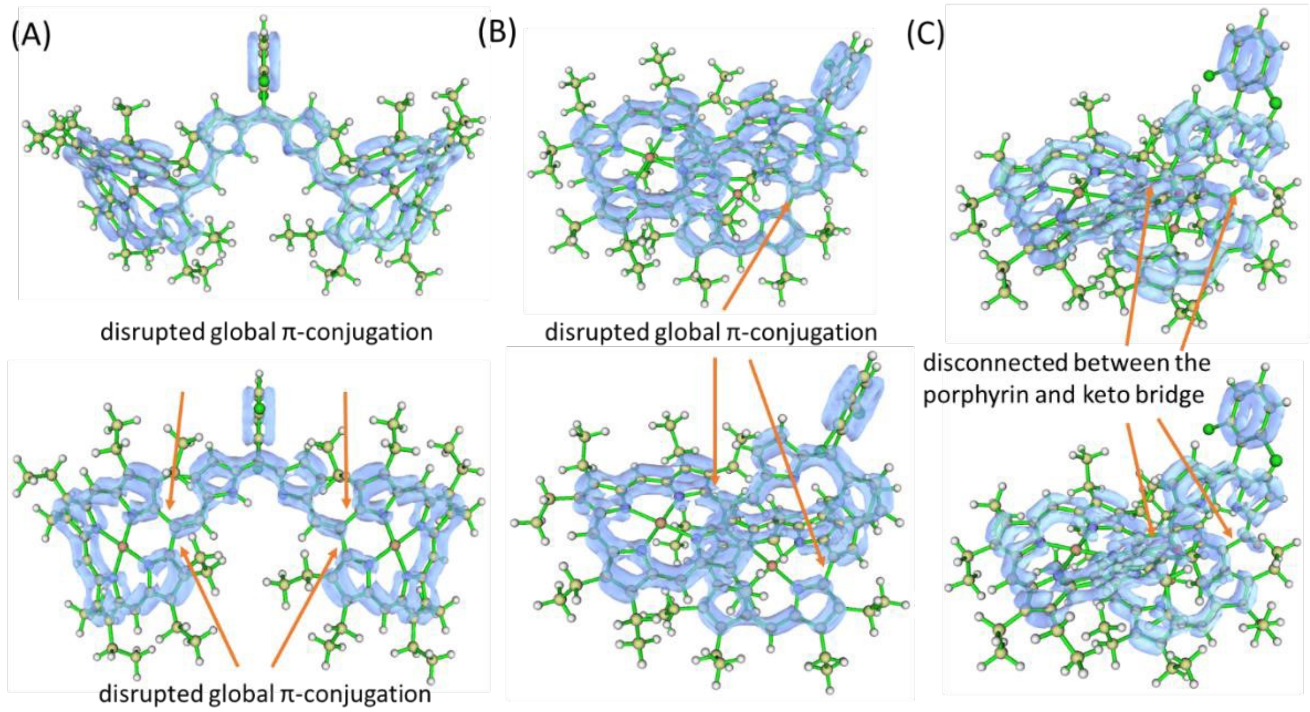

Figure 13. LOL-π isosurface map of (A) [**2**•Ni]$^+$ (top) and [**2**•Ni]$^{2+}$ (bottom); (B) [**3**•Ni]$^+$ (top) and [**3**•Ni]$^{2+}$ (bottom); (C) [**4**•Ni]$^+$ (top) and [**4**•Ni]$^{2+}$ (bottom), with iso-value of 0.45 a.u.

View Article Online
DOI: 10.1039/D5QI01175C

carbonyl bridges in **4**•M resulted in less intense NIR bands than **2**•M.

Notably, upon oxidation of **2**•M and **3**•M, a disrupted global 18π-conjugation in both porphyrin macrocycles was visualized in the LOL-π isosurface map, indicating the contribution from the potentially quinoidal porphyrin-like structures (Figure 13, traces A and B).[26b,c] The resulting structures could produce effective electronic interactions through the dipyrrin moieties. In the case of oxidized **4**•M, a disrupted electronic conjugation between porphyrin macrocycles was observed in the LOL-π isosurface, likely due to the presence of a discrete carbonyl resonant structure between the dipyrrin and porphyrin units (Figure 13C).

Kohn-Sham orbital profile of neutral complexes highlights the smaller HOMO–LUMO gaps in the case of **4**•M followed by **2**•M and **3**•M. Interestingly, the LUMO in **4**•Cu is much more stabilized, leading to a significant decrease in the HOMO–LUMO energy gap. This qualitatively explains the observed large red-shift of the NIR band in the electronic spectroscopy. A similar trend was observed in nickel complexes (Figures 14 and S43).

Upon oxidation of **2**•M, **3**•M, and **4**•M, the Kohn-Sham orbital profiles of 1e⁻- and 2e⁻-oxidised complexes revealed the notable electronic coefficients and spin delocalization through the bridge. After stepwise oxidation, HOMO–LUMO gaps are further tuned due to changes in electronic coefficients and spin delocalization via the bridge (Figures 15 and S44–S45). As observed in the neutral complexes, HOMO–LUMO gaps of the 1e⁻-oxidized complexes follow the same order: $[\mathbf{4}\bullet\mathrm{M}]^+ < [\mathbf{3}\bullet\mathrm{M}]^+ < [\mathbf{2}\bullet\mathrm{M}]^+$. This also qualitatively explains the observed red-shift of the NIR band in the electronic spectroscopy. For the 2e⁻ oxidised species, however, the HOMO–LUMO gap follows the opposite order $[\mathbf{2}\bullet\mathrm{M}]^{2+} < [\mathbf{3}\bullet\mathrm{M}]^{2+} < [\mathbf{4}\bullet\mathrm{M}]^{2+}$, which qualitatively explains the observed blue-shift of the NIR band. This also highlights the importance of the molecular shapes along with the conjugation pathway.

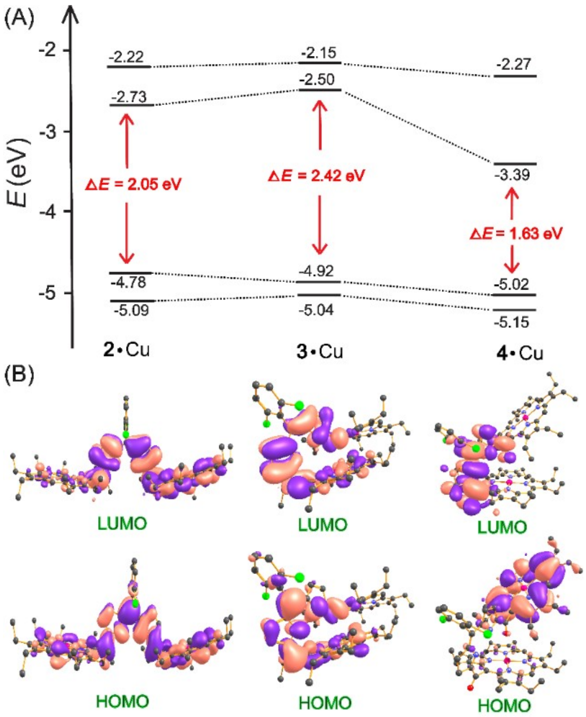

Figure 14. (A) Energy profile of **2**•Cu, **3**•Cu, and **4**•Cu; (B) Kohn-Sham orbital representations of the HOMOs and LUMOs (isovalue = 0.020).

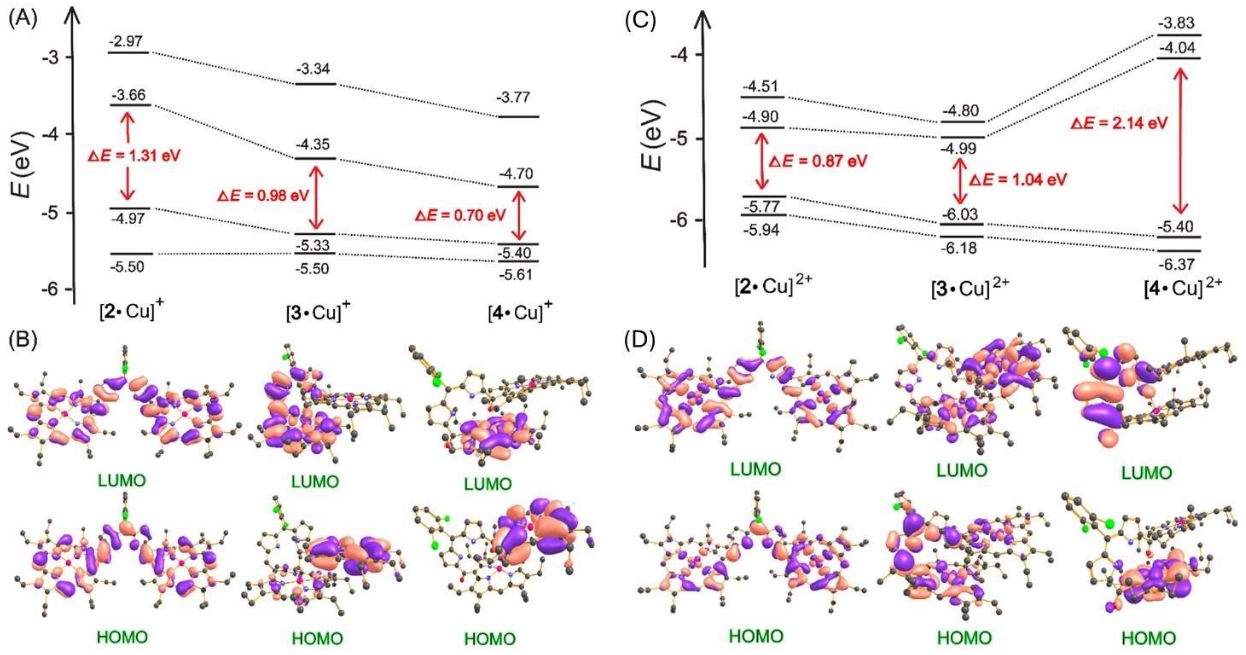

Figure 15. (A) Energy profile of $[\mathbf{2}\bullet\mathrm{Cu}]^+$, $[\mathbf{3}\bullet\mathrm{Cu}]^+$, and $[\mathbf{4}\bullet\mathrm{Cu}]^+$; (B) Kohn-Sham orbital representations of the HOMOs and LUMOs; (C) Energy profile of $[\mathbf{2}\bullet\mathrm{Cu}]^{2+}$, $[\mathbf{3}\bullet\mathrm{Cu}]^{2+}$, and $[\mathbf{4}\bullet\mathrm{Cu}]^{2+}$; (D) Kohn-Sham orbital representations of the HOMOs and LUMOs (isovalue = 0.020).

View Article Online
DOI: 10.1039/D5QI01135G

Conclusions

We demonstrate herein the shape-dependent intramolecular spin coupling through the conjugated bridge in dinickel(II) and dicopper(II) porphyrin dimers in neutral as well as in the oxidized complexes. The addition of DDQ at different concentrations to the unconjugated dimer, **1**•M (M = Ni, Cu), leads to various products that differ in their molecular shapes: *linear'* **2**•M, '*cofacially sloping*' **3**•M and '*clamshell bucket*' **4**•M. All the molecules have been isolated and structurally characterized. The presence of two carbonyl groups at the methine position of the dipyrrin bridge in **4**•Cu forces the porphyrin rings to move away from each other while one of the carbonyl oxygens is directed toward Cu(II) at a distance of 3.65 Å of another porphyrin ring. Mechanistic investigations using the ^{18}O isotope-labeled water (*i.e.*, $H_2{}^{18}O$) demonstrated that the carbonyl oxygen in **4**•M originated from the H_2O molecule. The extent of π-conjugation observed in the complexes was found to be dependent on the choice of the metal-ions and the molecular shape of the complexes. The highly π-conjugated nature and varying shapes of the porphyrin dimers resulted in several prominent attributes, including different colours and polarities, remarkably red-shifted and intense NIR absorption bands, and narrow HOMO–LUMO gaps, etc.

Notably, the addition of carbonyl moieties at the methine bridge in **4**•M facilitates stronger electronic communication through it. Kohn-Sham orbital profile of neutral complexes highlights the smaller HOMO–LUMO gaps in the case of **4**•M followed by **2**•M and **3**•M which has also been found directly correlated with the order of NIR bands observed experimentally. Indeed, the LUMO in **4**•M is much more stabilized, while π* orbital of the inserted carbonyl group effectively mediates the β to β bonding interaction, which resulted in a large red-shifted NIR absorption band with the narrowest HOMO–LUMO gap.

Upon stepwise oxidations by chemical oxidants, highly stable mono-cation radical and di-cation diradicals were isolated that exhibited long-range charge/radical delocalization via the bridge to produce strong NIR absorption bands. For $1e^{-}$-oxidized complexes, HOMO–LUMO gaps follow the order: [**4**•M]$^{+}$ < [**3**•M]$^{+}$ < [**2**•M]$^{+}$, which also qualitatively explains the observed trends of the NIR band in the electronic spectroscopy. For the $2e^{-}$-oxidised species, however, the HOMO–LUMO gap follows the opposite order [**2**•M]$^{2+}$ < [**3**•M]$^{2+}$ < [**4**•M]$^{2+}$, which again reproduces the experimental trends of the NIR bands. This highlights the importance of the molecular shapes along with the conjugation pathway.

The spin-density plots for the Cu(II) and Ni(II) porphyrin dimers in the neutral, $1e^{-}$-, and $2e^{-}$-oxidised states of **2**•M, **3**•M, and **4**•M demonstrate the significance and crucial role of metal ions, bridge, and their shape in the long-range electronic communication. The spin density plots display the distribution over the entire molecular framework with significant contributions to the bridging moiety in the $2e^{-}$-oxidised complexes of [**2**•M] and [**3**•M]. In contrast, no such spin distribution has been observed on the bridge in [**4**•M]$^{2+}$; rather spin density was completely localized on the porphyrin ring. As a result, π-conjugation between two macrocycles is better in linear '*butterfly-like*' followed by curved '*cofacially sloping*' and carbonyl-inserted '*clamshell bucket*', while nickel(II) dominates over copper(II) motifs. The observed $J_{r\text{-}r}$ exchange coupling for $2e^{-}$-oxidized complexes also follows the order. Triplet state EPR spectra were observed both in the solid as well as in the solution due to the magnetic interaction between the unpaired spins on the two Cu(II) centres. Indeed, the carbonyl group acts as a good π-mediator in [**4**•M]$^{2+}$ and is responsible for through space communication between the two porphyrin macrocycles. This has also been demonstrated in the non-covalent interaction between O atom and Cu (Cu•••O = 2.5 Å) in the complex supported by AIM analysis.

Data availability

A comprehensive description of the synthesis and experimental procedures, including full characterisation data, details of instrumentation, and computational methods, can be found in the Electronic Supplementary Information (ESI).

CCDC Numbers 2308954 (for **3**•Ni), 2444834 (for **4**•Cu·CH_2Cl_2) and 2444835 (for **4**•Cu·C_6H_{14}) contain the supplementary crystallographic data for this paper. These data can be obtained free of charge from the Cambridge Crystallographic Data Center *via* www.ccdc.cam.ac.uk/data_request/cif.

Author Contributions

SPR conceptualized and supervised the work. SJS and NG performed the experiments. SJS, RKT, GR and MI have done the DFT calculations. EG has analyzed the EPR results. HF and all the authors have analysed the results together and wrote the manuscript.

Conflicts of interest

There are no conflicts to declare.

Acknowledgements

We thank the Science and Engineering Research Board (SERB), India, SERB-STAR and CSIR, New Delhi, for financial support. SJS thank UGC for financial support. HF thanks the Anusandhan National Research Foundation (ANRF), Government of India for awarding him a Visiting Advanced Joint Research (VAJRA) faculty.

References

[1] (a) T. Tanaka and A. Osuka, Conjugated porphyrin arrays: synthesis, properties and applications for functional materials, *Chem. Soc. Rev.,* 2015, **44**, 943; (b) J. Yang, M.-C. Yoon, H. Yoo, P. Kim and D. Kim, Excitation energy transfer in multiporphyrin arrays with cyclic architectures: towards artificial light-harvesting antenna complexes, *Chem. Soc. Rev.*, 2012, **41**, 4808; (c) J. S. Lindsey and D. F. Bocian, Molecules for Charge-Based Information Storage, *Acc. Chem. Res.*, 2011, **44**, 638; (d) I. Beletskaya, V. S. Tyurin, A. Y. Tsivadze, R. Guilard and C. Stern, Supramolecular Chemistry of Metalloporphyrins, *Chem. Rev.*, 2009, **109**, 1659; (e) D. Gust, T. A. Moore and A. L. Moore, Solar Fuels via Artificial Photosynthesis, *Acc. Chem. Res.*, 2009, **42**, 1890; (f) N. Aratani, D. Kim and A. Osuka, Discrete Cyclic

View Article Online
DOI: 10.1039/D5QI01155C

Porphyrin Arrays as Artificial Light-Harvesting Antenna, *Acc. Chem. Res*., 2009, **42**, 1922.

[2] (a) V. S.-Y. Lin and S. G. DiMagno, Highly conjugated, acetylenyl bridged porphyrins: new models for light-harvesting antenna systems, *Science.,* 1994, **264**, 1105; (b) R. Wang, A. M. Brugh, J. Rawson, M. J. Therien and M. D. E. Forbes, Alkyne-Bridged Multi[Copper(II) Porphyrin] Structures: Nuances of Orbital Symmetry in Long-Range, Through-Bond Mediated, Isotropic Spin Exchange Interactions, *J. Am. Chem. Soc.,* 2017, **139**, 9759; (c) M. D. Peeks, C. E. Tait, P. Neuhaus, G. M. Fischer, M. Hoffmann, R. Haver, A. Cnossen, J. R. Harmer, C. R. Timmel and H. L. Anderson, Electronic Delocalization in the Radical Cations of Porphyrin Oligomer Molecular Wires**,** *J. Am. Chem. Soc*., 2017, **139**, 10461; (d) W. J. Cho, Y. Cho, S. K. Min, W. Y. Kim and K. S. Kim, Chromium porphyrin arrays as spintronic devices, *J. Am. Chem. Soc.,* 2011, **133**, 9364.

[3] (a) P. D. Harvey, C. Stern, C. P. Gros and R. Guilard, The photophysics and photochemistry of cofacial free base and metallated bisporphyrins held together by covalent architectures, *Coord. Chem. Rev*., 2007, **251**, 401; (b) J. Rosenthal, J. Bachman, J. L. Dempsey, A. J. Esswein, T. G. Gray, J. M. Hodgkiss, D. R. Manke, T. D. Luckett, B. J. Pistorio, A. S. Veige and D. G. Nocera, Oxygen and Hydrogen Photocatalysis by Two–Electron Mixed–Valence Coordination Compounds, *Coord. Chem. Rev*., 2005, **249**, 1316.

[4] (a) L. Xu, B. Wen, G. Kim, T. Kim, F. Cheng, M. Zhou, L. Xu, T. Tanaka, B. Yin, A. Osuka, D. Kim and J. Song, Strategic Construction of Directly Linked Porphyrin–BODIPY Hybrids, *Angew. Chem. Int. Ed*., 2017, **56**, 12322; (b) Y. Wu, M. Frasconi, D. M. Gardner, P. R. McGonigal, S. T. Schneebeli, M. R. Wasielewski and J. F. Stoddart, Electron Delocalization in a Rigid Cofacial Naphthalene-1,8:4,5-bis(dicarboximide) Dimer*, Angew. Chem., Int. Ed*., 2014, **53**, 9476.

[5] (a) X. Ma, E. A. Suturina, M. Rouzières, M. Platunov, F. Wilhelm, A. Rogalev, R. Clèrac and P. Dechambenoit, Using Redox-Active π Bridging Ligand as a Control Switch of Intramolecular Magnetic Interactions, *J. Am. Chem. Soc*., 2019, **141**, 7721; (b) X. Ma, E. A. Suturina, S. De, P. Nėgrier, M. Rouzières, R. Clèrac and P. Dechambenoit, A Redox-Active Bridging Ligand to Promote Spin Delocalization, High-Spin Complexes, and Magnetic Multi-Switchability**,** *Angew. Chem. Int. Ed.,* 2018, **57**, 7841; (c) J. Yoshida, K. Kuwahara, K. Suzuki and H. Yuge, Long-range intramolecular electronic communication in a trinuclear ruthenium tropolonate complex, *Inorg. Chem*., 2017, **56**, 1846; (d) D. M. D'Alessandro, Exploiting redox activity in metal–organic frameworks: concepts, trends and perspectives, *Chem. Commun*., 2016, **52**, 8957; (e) J. O. Moilanen, N. F. Chilton, B. M. Day, T. Pugh and R. A. Layfield, Strong Exchange Coupling in a Trimetallic Radical-Bridged Cobalt(II)-Hexaazatrinaphthylene Complex*, Angew. Chem. Int. Ed*., 2016, **55**, 5521.

[6] (a) C. Shu, H. Zhang, A. Olankitwanit, S. Rajca and A. Rajca, High-Spin Diradical Dication of Chiral π-Conjugated Double Helical Molecule**,** *J. Am. Chem. Soc*., 2019, **141**, 17287; (b) N. Gallagher, H. Zhang, T. Junghoefer, E. Giangrisostomi, R. Ovsyannikov, M. Pink, S. Rajca, M. B. Casu and A. Rajca, Thermally and Magnetically Robust Triplet Ground State Diradical, *J. Am. Chem. Soc*., 2019, **141**, 4764; (c) G. Moise, L. Tejerina, M. Rickhaus, H. L. Anderson and C. R. Timme, Spin Delocalization in the Radical Cations of Porphyrin Molecular Wires: A New Perspective on EPR Approaches, *J. Phys. Chem. Lett*., 2019, **10**, 5708.

[7] (a) M. Abe, Diradicals, *Chem. Rev*., 2013, **113**, 7011; (b) Z. Zeng, X. Shi, C. Chi, J. T. López Navarrete, J. Casado and J. Wu, Pro-aromatic and anti-aromatic π-conjugated molecules: an irresistible wish to be diradicals, *Chem. Soc. Rev*., 2015, **44**, 6578; (c) T. Kubo, Phenalenyl-Based Open-Shell Polycyclic Aromatic Hydrocarbons*, Chem. Rec*., 2015, **15**, 218; (d) T. Y. Gopalakrishna, W. Zeng, X. Lu and J. Wu, From open-shell singlet diradicaloids to polyradicaloids, *Chem. Commun*., 2018, **54**, 2186.

[8] (a) W. Kaim, A. Paretzki, Interacting metal and ligand based open shell systems: Challenges for experiment and theory, *Coord. Chem. Rev*., 2017, **344**, 345; (b) K. E. Preuss, Metal-radical coordination complexes of thiazyl and selenazyl ligands, *Coord. Chem. Rev*., 2015, **289**, 49; (c) M. Castellano, R. Ruiz-García, J. Cano, J. Ferrando-Soria, E. Pardo, F. R. Fortea-Pérez, S.-E. Stiriba, M. Julve and F. Lloret, Dicopper(II) Metallacyclophanes as Multifunctional Magnetic Devices: A Joint Experimental and Computational Study, *Acc. Chem. Res.,* 2015, **48**, 510; (d) K. E. Vostrikova, High-spin molecules based on metal complexes of organic free radicals, *Coord. Chem. Rev*., 2008, **252**, 1409.

[9] (a) N. Fukui, W. Cha, D. Shimizu, J. Oh, K. Furukawa, H. Yorimitsu, D. Kim and A. Osuka, Highly planar diarylamine-fused porphyrins and their remarkably stable radical cations**,** *Chem. Sci*., 2017, **8**, 189; (b) S. Richeter, C. Jeandon, N. Kyritsakas, R. Ruppert and H. J. Callot, Preparation of six isomeric bis-acylporphyrins with chromophores reaching the near-infrared via intramolecular Friedel-Crafts reaction, *J. Org. Chem*., 2003, **68**, 9200.

[10] (a) S. Sanfui, A. Roychowdhury, M. Usman, E. Garribba, C. J. Gómez-García and S. P. Rath, Metal *vs* Ligand Oxidation: Coexistence of Both Metal-Centered and Ligand-Centered Oxidized Species *Inorg. Chem.* 2024, **63**, 5423; (b) A. Kumar, M. Usman, D. Samanta and S. P. Rath, Through Bridge Spin Coupling in Homo- and Heterobimetallic Porphyrin Dimers upon Stepwise Oxidations: A Spectroscopic and Theoretical Investigation. *Chem. Eur. J.,* 2021, **27**, 11428; (c) S. Dey, D. Sil and S. P. Rath, A Highly Oxidized Cobalt Porphyrin Dimer: Spin Coupling and Stabilization of the Four-Electron Oxidation Product*, Angew. Chem. Int. Ed.*, 2016, ***55***, 996; (d) D. Sil, S. Dey, A. Kumar, S. Bhowmik and S. P. Rath, Oxidation triggers extensive conjugation and unusual stabilization of two di-heme dication diradical intermediates: role of bridging group for electronic communication**,** *Chem. Sci.*, 2016, **7**, 1212; (e) S. Dey, D. Sil, Y. A. Pandit, and S. P. Rath, Effect of Two Interacting Rings in Metalloporphyrin Dimers upon Stepwise Oxidations. *Inorg. Chem.* 2016, **55***,* 3229.

[11] (a) Y. Terazono, G. Kodis, M. Chachisvilis, B. R. Cherry, M. Fournier, A. Moore, T. A. Moore and D. Gust, Multiporphyrin arrays with π-π interchromophore interactions**,** *J. Am. Chem. Soc.,* 2015, **137**, 245; (b) J. Zeng, K and -Q. Chen, Spin filtering, magnetic and electronic switching behaviors in manganese porphyrin-based spintronic devices, *J. Mater. Chem. C.,* 2013, **1**, 4014; (c) M. S. Choi, T. Yamazaki, I. Yamazaki and T. Aida, Bioinspired Molecular Design of Light-Harvesting Multiporphyrin Arrays, *Angew. Chem. Int. Ed.,* 2004, **43**, 150.

[12] (a) S. Demir, I.-R. Jeon, J. R. Long and T. D. Harris, Radical ligand-containing single-molecule magnets, *Coord. Chem. Rev*., 2015, **289**, 149; (b) T. J. Dunn, L. Chiang, C. F. Ramogida, K. Hazin, M. I. Webb, M. J. Katz and T. Storr, Class III Delocalization and Exciton Coupling in a Bimetallic Bis-ligand Radical Complex*, Chem. Eur. J*., 2013, **19**, 9606; (c) O. Gidron, Y. Diskin-Posner and M. Bendikov, High Charge Delocalization and Conjugation in Oligofuran Molecular Wires*, Chem. Eur. J*., 2013, **19**, 13140; (d) J. D. Rinehart, M. Fang, W. J. Evans, J. R. Long, AN$_2^{3-}$ Radical-Bridged Terbium Complex Exhibiting Magnetic Hysteresis at 14 K, *J. Am. Chem. Soc.,* 2011, **133**, 14236; (e) A. K. Das, B. Sarkar, J. Fiedler, S. Zális, I. Hartenbach,

S. Strobel, G. K. Lahiri and W. Kaim, A Five-Center Redox System: Molecular Coupling of Two Noninnocent Imino-*o*-benzoquinonato-Ruthenium Functions through a π Acceptor Bridge, *J. Am. Chem. Soc*., 2009, **131**, 8895.

[13] (a) S. Banerjee; N. Awasthi; A. Roychowdhury; D. Samanta; P. Arora; N. Dutta; A. Draksharapu, E. Garribba and S. P. Rath, Electron Shuttling in High-Valent Heterobimetallic NiFe-Porphyrin Dimers: Stabilization of Ni(III) and Fe-Phenoxyl Radicals, *Inorg. Chem.,* 2025, **64**, 5431; (b) A. K. Singh and S. P. Rath, Intermacrocyclic Interactions upon Stepwise Oxidations in a Monometallic Porphyrin Dimer: Ring versus Metal-Center Oxidations and Effect of Counter Anions, *Chem. Eur. J.,* 2020, **26**, 14405; (c) A. Kumar, S. Sanfui, G. Sciortino, J.-D. Marechal, E. Garribba and S. P. Rath, Stepwise Oxidations in a Cofacial Copper(II) Porphyrin Dimer: Through-Space Spin-Coupling and Interplay between Metal and Radical Spins, *Chem. Eur. J*., 2020, **26**, 7869.

[14] (a) Y. A. Pandit, S. J. Shah, M. Usman, S. Sarkar, E. Garribba and S. P. Rath, Long-Range Intramolecular Spin Coupling through a Redox-Active Bridge upon Stepwise Oxidations: Control and Effect of Metal Ions, *Inorg. Chem*., 2022, **61**, 5270; (b) S. J. Shah, A. Singh, D. Goswami, M. Ishida and S. P. Rath, Reversible open–closed conformational switching of nano-size metalloporphyrin dimers triggered by light and temperature, *Dalton Trans.,* 2024, **53**, 6758.

[15] S. J. Shah, Y. A. Pandit, E. Garribba. M. Ishida and S. P. Rath, Stable Dication Diradicals of Triply Fused Metallo Chlorin-Porphyrin Heterodimers: Impact of the Bridge on the Control of Spin Coupling to Reactivity*, Chem. Eur. J.,* 2023, **29**, e2023019.

[16] (a) Z. Chen, C. S. Wannere, C. Corminboeuf, R. Puchta and P. V. R. Schleyer, Nucleus-Independent Chemical Shifts (NICS) as an Aromaticity Criterion, *Chem. Rev.,* 2005, **105**, 3842; (b) D. Geuenich, K. Hess, F. Köhler and R. Herges, Anisotropy of the induced current density (ACID), a general method to quantify and visualize electronic delocalization, *Chem. Rev.,* 2005, **105**, 3758; (c) S. N. Steinmann, Y. Mo and C. Corminboeuf, How do electron localization functions describe π-electron delocalization?, *Phys. Chem. Chem. Phys*., 2011, **13**, 20584.

[17] N. Fukui, T. Kim, D. Kim and A. Osuka, Porphyrin Arch-Tapes: Synthesis, Contorted Structures, and Full Conjugation, *J. Am. Chem. Soc*., 2017, **139**, 9075.

[18] (a) M. Li, T. J. Neal, G. R. A. Wyllie, A. G. Oliver, C. E. Schulz and W. R. Scheidt, Metalloporphyrin Mixed-Valence π-Cation Radicals: $[\mathrm{Fe(oxoOEC^{\bullet/2})\text{-}(Cl)}]_2\mathrm{SbCl_6}$, Structure, Magnetic Properties, and Near-IR Spectra, *Inorg. Chem*., 2011, **50**, 9114; (b) M. Li, T. J. Neal, G. R. A. Wyllie, A. G. Oliver, C. E. Schulz and W. R. Scheidt, Structural and Magnetic Effects of meso-Substitution in Alkyl-SubstitutedMetalloporphyrinate π-Cation Radicals: Characterization of $[\mathrm{Fe(TalkylP^{\bullet})(Cl)}]\mathrm{SbCl_6}$ (alkyl = ethyl and n-propyl)*, Inorg. Chem*., 2010, **49**, 8078; (c) S. Hu and T. G. Spiro, The Origin of Infrared Marker Bands of Porphyrin x-Cation Radicals: Infrared Assignments for Cations of Copper(II) Complexes of Octaethylporphine and Tetraphenylporphine, *J. Am. Chem. Soc*., 1993, **115**, 12029.

[19] D. L. Sun, S. V. Rosokha, S. V. Lindeman and J. K. Kochi, Intervalence (charge-resonance) transitions in organic mixed-valence systems. Through-space versus through-bond electron transfer between bridged aromatic (redox) centers, *J. Am. Chem. Soc*., 2003, **125**, 15950; (b) A. Takai, M. Chkounda, A. Eggenspiller, C. P. Gros, M. Lachkar, J.-M. Barbe and S. Fukuzumi, Efficient Photoinduced Electron Transfer in a Porphyrin Tripod−Fullerene Supramolecular Complex via π−π Interactions in Nonpolar Media, *J. Am. Chem. Soc.,* 2010, **132**, 4477; (c) Z. Cong, T. Kurahashi and H. Fujii, Oxidation of Chloride and Subsequent Chlorination of Organic Compounds by Oxoiron(IV) Porphyrin p-Cation Radicals, *Angew. Chem. Int. Ed.,* 2011, **50**, 9935.

[20] M. J. Frisch, G. W. Trucks, H. B. Schlegel, G. E. Scuseria, M. A. C. Robb, J. R. Cheeseman, G. Scalmani, V. Barone, G. A. N. B. Mennucci, H. Petersson, M. Caricato, X. Li, H. Hratchian, A. F. Izmaylov, J. Bloino, G. Zheng, J. L. Sonnenberg, M. Hada, M. Ehara, K. Toyota, R. Fukuda, J. Hasegawa, M. Ishida, Y. K. T. Nakajima, O. Honda, H. Nakai, T. Vreven, J. A. Montgomery, J. E. O. Peralta, F. Oligaro, M. Bearpark, J. J. Heyd, E. Brothers, V. N. Kudin, K. K. N. R. Staroverov, J. Normand, K. Raghavachari, A. B. Rendell, S. S. Iyengar, J. Tomasi, M. Cossi, J. M. Rega, M. Millam, J. E. Knox, J. B. Cross, V. Bakken, C. J. Adamo, J. Gomperts, R. E. Stratmann, O. Yazyev, A. J. Austin, R. Cammi, J. W. Pomelli, J. W. Ochterski, R. L. Martin, K. Z. Morokuma, V. G. Zarkrzewski, G. A. Voth, P. Salvador, J. J. D. Dannenberg, S. Dapprich, A. D. Daniels, Ö. Farkas, J. B. Foresman, J. V. Ortiz, J. Cioslowski and D. J. Fox, Gaussian 16, Revision C.01, Gaussian, Inc., Wallingford, CT, 2016.

[21] N. F. Chilton, R. P. Anderson, L. D. Turner, A. Soncini and K. S. Murray, PHI: A powerful new program for the analysis of anisotropic monomeric and exchange-coupled polynuclear *d*- and *f*-block complexes, *J. Comput. Chem.*, 2013, **34**, 1164.

[22] (a) S. Sarkar, R. K. Tiwari, D. Samanta, T. Guchhait, E. C. Sañudo, G. Rajaraman and S. P. Rath, Unusual Stabilisation of Remarkably Bent Tetra-Cationic Tetra-radical Intermolecular Fe(III) μ-Oxo Tetranuclear Complexes, *Angew. Chem. Int. Ed*., 2024, **63**, e202402344; (b) S. K. Singh and G. Rajaraman, Can Anisotropic Exchange Be Reliably Calculated Using Density Functional Methods? A Case Study on Trinuclear $\mathrm{Mn^{III}}$-$\mathrm{M^{III}}$-$\mathrm{Mn^{III}}$ (M=Fe, Ru, and Os) Cyanometalate Single-Molecule Magnets*, Chem. Eur. J.,* 2014, **20**, 113.

[23] (a) B. J. Hathaway and D. E. Billing, The electronic properties and stereochemistry of mono-nuclear complexes of the copper(II) ion, *Coord. Chem. Rev*., 1970, **5**, 143; (b) B. J. Hathaway, A new look at the stereochemistry and electronic properties of complexes of the copper(II) ion**,** *Struct. Bonding (Berlin).,* 1984, **57**, 55; (c) E. Garribba and G. *J.* Micera, The Determination of the Geometry of Cu(II) Complexes: An EPR Spectroscopy Experiment, *J. Chem. Educ*., 2006, **83**, 1229.

[24] (a) K. L. Cunningham, K. M. McNett, R. A. Pierce, K. A. Davis, H. H. Harris, D. M. Falck and D. R. McMillin, EPR Spectra, Luminescence Data, and Radiationless Decay Processes of Copper(II) Porphyrins, *Inorg. Chem.,* 1997, **36**, 608; (b) N. Wili, S. Richert, B. Limburg, S. J. Clarke, H. L. Anderson, C. R. Timmel and G. Jeschk, ELDOR-detected NMR beyond hyperfine couplings: a case study with Cu(II)-porphyrin dimers**,** *Phys. Chem. Chem. Phys*., 2019, **21**, 11676.

[25] (a) T. D. Smith and J. R. Pilbrow, *Coord. Chem. Rev*., 1974, **13**, 173; (b) R. S Drago, *Physical Methods in Chemistry*. W. B. Saunders Company: Philadelphia, 1977, p. 343; (c) J. R. Pilbrow, *Transition Ion Electron Paramagnetic Resonance*. Clarendon Press: Oxford, 1990, p. 332.

[26] (a) J. Rawson, P. J. Angiolillo and M. J. Therien, Extreme electron polaron spatial delocalization in π-conjugated materials**,** *Proc. Natl. Acad. Sci. USA.,* 2015**, 112**, 13779; (b) C. Li, L. Zhu, W. Liang, R. Su, J. Yin, Y. Hu, Y. Lan, D. Wu and J. You, An unusual [4 + 2] fusion strategy to forge *meso-N/O*-heteroarene-fused (quinoidal) porphyrins with intense near-infrared Q-bands, *Chem. Sci*., 2019, **10**, 7274; (c) K. Yamasumi, Y. Notsuka, Y. Yamaoka, S. Mori, M. Ishida and H. Furuta, Synthesis of Helically π-Extended N-Confused Porphyrin Dimer via *meso*-Bipyrrole-Bridge with Near-Infrared-II Absorption Capability, *Chem. Eur. J.,* 2020, **26**, 13590.

DOI: 10.1039/D5QI01135C

Data availability

View Article Online
DOI: 10.1039/D5QI01135C

The data supporting this article have been included as part of the Supplementary Information.